

Estimation of spatial distribution and fluid fraction of a potential supercritical geothermal reservoir by magnetotelluric data: a case study from Yuzawa geothermal field, NE Japan

Keiichi Ishizu¹, Yasuo Ogawa¹, Keishi Nunohara², Noriyoshi Tsuchiya³, Masahiro Ichiki³, Hideaki Hase⁴, Wataru Kanda¹, Shinya Sakanaka⁵, Yoshimori Honkura⁶, Yuta Hino¹, Kaori Seki⁷, Kuo Hsuan Tseng⁸, Yusuke Yamaya⁹, and Toru Mogi¹

¹Volcanic Fluid Research Center, Tokyo Institute of Technology

²Graduate School of Environmental Studies, Tohoku University

³Tohoku University

⁴Geothermal Energy Research & Development Co., Ltd.

⁵Unknown

⁶Tokyo Institute of Technology, Volcanic Fluid Research Center

⁷Kokusai Kogyo Co., Ltd.

⁸Department of Earth and Planetary Sciences, Tokyo Institute of Technology

⁹Fukushima Renewable Energy Institute, AIST

November 24, 2022

Abstract

Magmatic fluids within the crust may exist under supercritical conditions (e.g. $>374^{\circ}\text{C}$ and >22.1 MPa for pure water). Geothermal systems using such supercritical fluids have gained attention as unconventional geothermal resources because they can offer significantly more energy than conventional geothermal fluids with temperatures $<350^{\circ}\text{C}$. Although an understanding of the spatial distribution and fluid fraction of supercritical geothermal reservoirs is necessary for their resource assessment, the spatial distribution and fluid fraction of supercritical geothermal reservoirs worldwide are poorly understood due to the limited number of geophysical observations. Here, the magnetotelluric (MT) method with electrical resistivity imaging was used in the Yuzawa geothermal field, northeastern Japan, to obtain information on the fluid fraction and spatial distribution of a supercritical geothermal reservoir. Our MT data revealed a potential supercritical geothermal reservoir ($>400^{\circ}\text{C}$) with a horizontal dimension of 3 km (width) \times 5 km (length) at a depth of 2.5–6 km. The estimated fluid fraction of the supercritical reservoir was 0.5–2% with a salinity of 5–10 wt%. The melt was imaged below a supercritical geothermal reservoir. Based on the resistivity model, we propose a mechanism for the evolution of a supercritical fluid reservoir, wherein upwelling supercritical fluids supplied from the melt are trapped under less permeable silica sealing. As a result, supercritical fluids accumulate under the silica sealing. This study is the first to present a detailed estimation of the spatial distribution and fluid fraction of a potential supercritical geothermal reservoir.

Hosted file

jgr_si_2021_0806_ki.docx available at <https://authorea.com/users/476513/articles/602637-estimation-of-spatial-distribution-and-fluid-fraction-of-a-potential-supercritical-geothermal-reservoir-by-magnetotelluric-data-a-case-study-from-yuzawa-geothermal-field-ne-japan>

1 **Estimation of spatial distribution and fluid fraction of a potential supercritical**
2 **geothermal reservoir by magnetotelluric data: a case study from Yuzawa**
3 **geothermal field, NE Japan**
4

5 **Keiichi Ishizu¹, Yasuo Ogawa¹, Keishi Nunohara², Noriyoshi Tsuchiya², Masahiro Ichiki³,**
6 **Hideaki Hase^{1,6}, Wataru Kanda¹, Shinya Sakanaka⁴, Yoshimori Honkura¹, Yuta Hino¹,**
7 **Kaori Seki^{1,7}, Kuo Hsuan Tseng^{1,8}, Yusuke Yamaya⁵, and Toru Mogi¹**

8 ¹ Volcanic Fluid Research Center, Tokyo Institute of Technology, Tokyo, Japan

9 ² Graduate School of Environmental Studies, Tohoku University, Miyagi, Japan

10 ³ Graduate School of Science, Tohoku University, Miyagi, Japan

11 ⁴ Graduate School of International Resource Sciences, Akita University, Akita, Japan

12 ⁵ Fukushima Renewable Energy Institute, National Institute of Advanced Industrial Science and
13 Technology, Fukushima, Japan

14 ⁶ Now at Geothermal Energy Research & Development Co., Ltd., Tokyo, Japan

15 ⁷ Now at Groundwater and Hydrology Group, Kokusai Kogyo Co., Ltd., Tokyo, Japan

16 ⁸ Now at Sumiko Resources Exploration & Development Co., Ltd., Tokyo, Japan

17
18 Corresponding author: Keiichi Ishizu (ishizu.k.ab@m.titech.ac.jp)

19
20 **Key points:**

- 21 • A supercritical geothermal reservoir of 3 km (width) × 5 km (length) was imaged by the
22 magnetotelluric method at a depth of 2.5–6 km.
- 23 • The fluid fraction of the supercritical reservoir was estimated to be 0.5–2% with a salinity
24 of 5–10 wt%.
- 25 • Upwelling supercritical fluids supplied from the melt were trapped under a less-
26 permeable silica sealing.

27
28 **Abstract**

29 Magmatic fluids within the crust may exist under supercritical conditions (e.g. >374°C and >22.1
30 MPa for pure water). Geothermal systems using such supercritical fluids have gained attention as
31 unconventional geothermal resources because they can offer significantly more energy than
32 conventional geothermal fluids with temperatures <350°C. Although an understanding of the
33 spatial distribution and fluid fraction of supercritical geothermal reservoirs is necessary for their
34 resource assessment, the spatial distribution and fluid fraction of supercritical geothermal
35 reservoirs worldwide are poorly understood due to the limited number of geophysical
36 observations. Here, the magnetotelluric (MT) method with electrical resistivity imaging was used

37 in the Yuzawa geothermal field, northeastern Japan, to obtain information on the fluid fraction
38 and spatial distribution of a supercritical geothermal reservoir. Our MT data revealed a potential
39 supercritical geothermal reservoir ($>400^{\circ}\text{C}$) with a horizontal dimension of 3 km (width) \times 5 km
40 (length) at a depth of 2.5–6 km. The estimated fluid fraction of the supercritical reservoir was
41 0.5–2% with a salinity of 5–10 wt%. The melt was imaged below a supercritical geothermal
42 reservoir. Based on the resistivity model, we propose a mechanism for the evolution of a
43 supercritical fluid reservoir, wherein upwelling supercritical fluids supplied from the melt are
44 trapped under less permeable silica sealing. As a result, supercritical fluids accumulate under the
45 silica sealing. This study is the first to present a detailed estimation of the spatial distribution and
46 fluid fraction of a potential supercritical geothermal reservoir.

47

48 **Plain language summary**

49 As the demand for clean, renewable energy increases worldwide, geothermal energy has
50 emerged as a clean and renewable energy source. Subsurface fluids in a supercritical state (high
51 temperature and pressure of $>374^{\circ}\text{C}$ and >22.1 MPa) have gained attention as next-generation
52 geothermal resources because they can offer significantly more energy than conventional
53 geothermal fluids with temperatures $<350^{\circ}\text{C}$. Supercritical geothermal fluids are believed to be
54 found in various volcanic areas worldwide. Although an understanding of the spatial distribution
55 and fluid fraction of supercritical fluids is necessary for their resource assessment, the spatial
56 distribution and fluid fraction of supercritical geothermal reservoirs are poorly understood.
57 Therefore, we used the magnetotelluric (MT) method to obtain information on the spatial
58 distribution and fluid fraction of a supercritical geothermal reservoir in the Yuzawa geothermal
59 field, northeastern Japan. Our MT data revealed a potential supercritical geothermal reservoir of
60 3 km (width) \times 5 km (length) at a depth of 2.5–6 km with a fluid fraction estimated to be 0.5–2%
61 and a salinity of 5–10 wt%. This study presents the first detailed estimation of the spatial
62 distribution and fluid fraction of a potential supercritical geothermal reservoir.

63

64 **1. Introduction**

65 Magmatic fluids with high temperatures may exist in a supercritical state (e.g. $>374^{\circ}\text{C}$ and >22.1
66 MPa for pure water, and $>406^{\circ}\text{C}$ and >29.8 MPa for seawater salinity) at a depth of about 2–10
67 km beneath volcanic areas (Bali et al., 2020; Fournier, 1999; Friðleifsson et al., 2020; Ikeuchi et
68 al., 1998; Reinsch et al., 2017; Scott et al., 2015; Tsuchiya et al., 2016). In fact, several deep
69 drilling expeditions have found magmatic fluid in a supercritical state. An exploration well (WD-
70 1a) in the Kakkonda geothermal area in northeastern (NE) Japan found magmatic fluid at 500°C
71 at a depth of 3729 m (Doi et al., 1998; Ikeuchi et al., 1998), wherein the fluid at the bottom of the
72 well was under supercritical conditions (Saishu et al., 2014; Tsuchiya & Hirano, 2007). Similarly,
73 an exploratory well drilled by the Iceland Deep Drilling Project (IDDP) also encountered a
74 reservoir of supercritical fluids at a temperature of 450°C in the Krafla volcanic system (Elders
75 et al., 2014; Scott et al., 2015).

76 Geothermal systems using supercritical fluids have recently gained attention as next-generation
77 geothermal resources (Friðleifsson et al., 2020; Okamoto et al., 2019; Parisio et al., 2019;
78 Reinsch et al., 2017; Stimac et al., 2017; Watanabe et al., 2017). Various countries, including
79 Japan, the USA, New Zealand, and Italy, are beginning to consider the development of power

80 plants using supercritical fluids (Reinsch et al., 2017).. This newfound attention comes from the
81 fact that supercritical fluids have significant advantages as a source of energy: a higher enthalpy
82 per unit mass and a lower fluid viscosity than conventional geothermal fluids with temperatures
83 $<350^{\circ}\text{C}$ (Reinsch et al., 2017). Power generation systems using supercritical fluids are therefore
84 able to a large output from a single power plant. A test of the capacity of supercritical fluids
85 (wellhead temperature of 450°C) from IDDP-1 in Krafla revealed that the energy output was 10-
86 fold higher than that of conventional wells (Elders et al., 2014).

87 Gaining an in-depth understanding of the spatial distribution and fluid fraction of supercritical
88 geothermal reservoirs is necessary for their assessment as an unconventional energy resource
89 (Reinsch et al., 2017; Stimac et al., 2017). Deep drilling can be used to calculate the amount of
90 available resources of supercritical fluids (Doi et al., 1998; Elders et al., 2014; Fournier, 1999;
91 Friðleifsson et al., 2020; Ikeuchi et al., 1998). In one drill expedition, a core sample of the
92 Kakkonda granite in the WD-1a well near the bottom (3729 m depth) was found to have a
93 porosity of 1.7% (Muraoka et al., 1998). However, as a method to assess supercritical
94 geothermal systems, deep drillings are expensive (Elders et al., 2014). Owing to the limited
95 number of deep drilling points, the distribution and fluid fraction of supercritical geothermal
96 reservoirs remain poorly understood. Therefore, geophysical methods (e.g. electromagnetic and
97 seismic methods) are required to gain insights into the spatial distribution and fluid fraction of
98 supercritical geothermal reservoirs (Piana Agostinetti et al., 2017; Reinsch et al., 2017).

99 In this study, we used the magnetotelluric (MT) method with electrical resistivity imaging to
100 calculate the spatial distribution and fluid fraction of a supercritical geothermal reservoir in NE
101 Japan. The MT method is suitable for measuring the spatial distribution and fluid fraction of
102 subsurface fluids because electrical resistivity is sensitive to the existence of fluids (Comeau et
103 al., 2020; Ogawa et al., 2014; Unsworth et al., 2005; Wannamaker et al., 2009). The fluid
104 fraction of a supercritical geothermal reservoir was obtained from a resistivity model using MT
105 data. For the estimation of the fluid fraction, we assumed that the supercritical geothermal
106 reservoir consisted of solid rock and supercritical fluid in the solid-rock pore, and that the
107 supercritical fluid saturated the pore. The resistivity obtained using the MT method is bulk
108 resistivity, which includes contributions from the solid rock and supercritical fluid in the pore
109 (Chave & Jones, 2012; Hashin & Shtrikman, 1962). However, the contribution of solid rock
110 resistivity to bulk resistivity is limited (Ogawa et al., 2014), indicating that if the resistivity of a
111 supercritical fluid is known, we can obtain the fluid fraction of a supercritical geothermal
112 reservoir from the bulk resistivity. We considered magmatic supercritical fluids as NaCl-H₂O
113 fluids because magmatic fluids mainly consist of water and chloride salts (Blundy et al., 2021;
114 Heinrich, 2005; Monecke et al., 2018; Richards, 2011; Sillitoe, 2010). The electrical resistivity
115 of NaCl-H₂O fluids has been studied extensively in the relationship between subsurface
116 resistivity models and geological structures (Bannard, 1975; Nono et al., 2020; Quist & Marshall,
117 1968; Sakuma & Ichiki, 2016; Sinmyo & Keppler, 2016). Bannard (1975) measured the
118 resistivity of NaCl-H₂O fluids for a wide range of pressure, temperature, and NaCl conditions,
119 including supercritical conditions (up to 200 MPa, 525°C , and 25 wt%). Thus, we used the
120 resistivity values of NaCl-H₂O fluids reported by Bannard (1975) for the resistivity of
121 supercritical fluids.

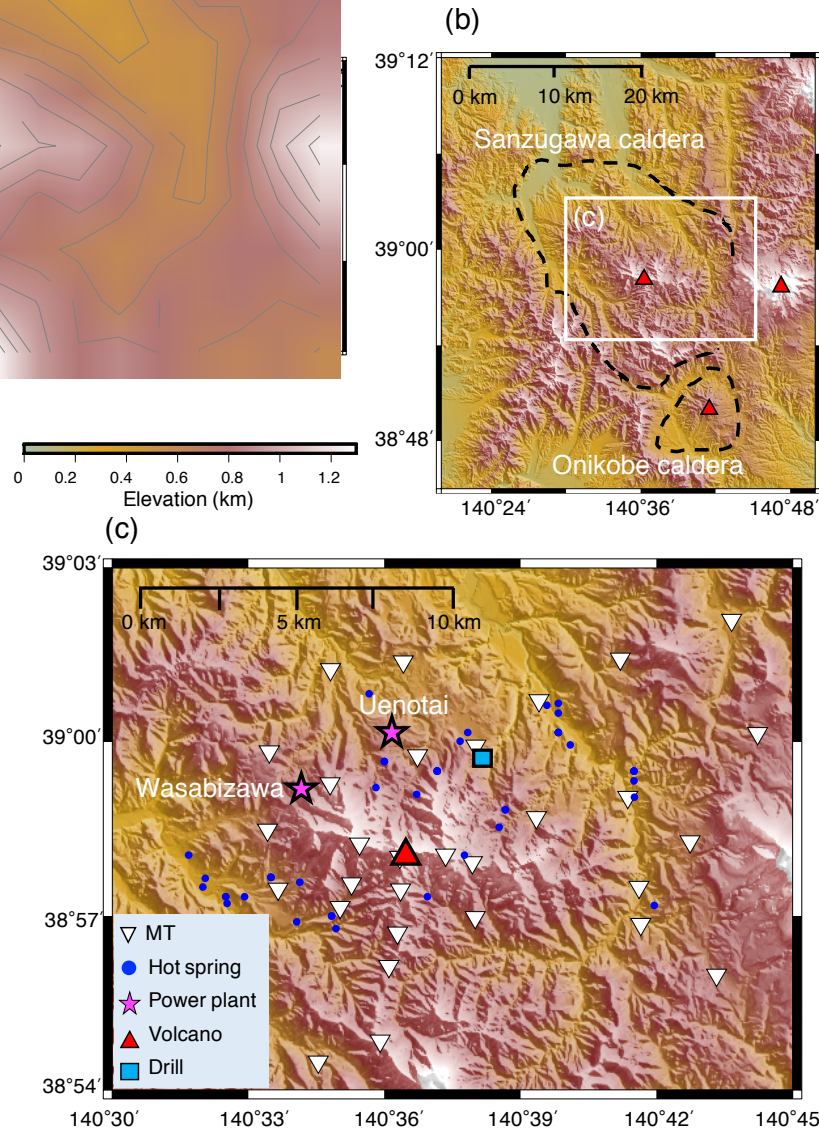
122 NE Japan can be classified as a typical subduction zone, where the Pacific plate subducts beneath
123 the land area at a rate of ~ 10 cm/year (Hasegawa et al., 1991). The dehydration of the
124 subducting slab in the mantle wedge results in the upward migration of fluids (Tatsumi, 1989).

125 Upwelling hot fluids from the mantle wedge were detected by low-velocity anomalies of S-wave
126 (so-called “hot fingers”). These hot fingers are distributed over NE Japan at intervals of several
127 tens of kilometers (Tamura et al., 2002) and indicate that a large number of supercritical fluid
128 reservoirs may exist in NE Japan (Okamoto et al., 2019). We selected the Yuzawa geothermal
129 field in NE Japan as the target area. Hot fingers exist around this geothermal field (Tamura et al.,
130 2002). Other geophysical and geochemical data (e.g. thermoluminescence, borehole temperature,
131 and seismic data) also suggest that supercritical fluids may exist at a depth of a few kilometers
132 (New Energy and Industrial Technology Development Organization, 1990; Nunohara et al.,
133 2021; Okada et al., 2014). We conducted an MT survey to reveal the spatial distribution and
134 fluid fraction of a potential supercritical geothermal reservoir in this field. Any information
135 obtained on a supercritical geothermal reservoir in this field is likely to be useful for the
136 estimation of spatial distribution and fluid fraction of other supercritical geothermal reservoirs in
137 NE Japan (e.g. Naruko, Onikobe, and Kakkonda areas). Here, we first provide a brief
138 introduction of the Yuzawa geothermal field and MT method. Then, we present our findings on
139 the estimation of the spatial distribution of a potential supercritical reservoir and its fluid fraction.
140

141 **2. Yuzawa geothermal field in NE Japan**

142 The Yuzawa geothermal field in NE Japan contains one of the largest geothermal systems in
143 Japan (Nunohara et al., 2021). This field is located in the inner part of the Sanzugawa caldera
144 (Figures 1a and 1b). The Sanzugawa caldera, which was first formed ca. 3 My ago, has a size of
145 30 km north-south and 20 km east-west (Takeno, 2000). A Quaternary volcano, the Takamatsu
146 volcano, or Takamatsu-dake, is found in this geothermal field (red star in Figures 1b and 1c).
147 The Takamatsu volcano is located 40 km west of the volcanic front (Tamanyu et al., 1998). The
148 volcano is composed of calc-alkaline andesite to dacite. The age of this volcano was estimated to
149 be 0.2–0.3 My by thermo-luminescence and K–Ar methods (Umeda et al., 1999). The magma
150 below the volcano is considered to be the heat source of this geothermal field (Takeno, 2000).
151 Geothermal features, such as hot springs and hydrothermally altered rocks, have been observed
152 extensively at the surface in this geothermal field, indicative of a well-developed hydrothermal
153 system (Nunohara et al., 2021). Two geothermal power plants (Uenotai: 28,500 kW and
154 Wasabizawa: 46,200 kW) are currently in operation using a hydrothermal system at temperatures
155 <300°C (Figure 1c).

156 Seismic imaging of NE Japan suggests that upwelling fluids exist beneath this geothermal field
157 at a depth of up to several kilometers (Nakajima et al., 2001; Okada et al., 2014; Tamura et al.,
158 2002). The high He^3/He^4 in this field also indicates that fluids upwell to the surface from the
159 upper mantle (Horiguchi et al., 2010; Kita et al., 1992). Drillings conducted by the New Energy
160 and Industrial Technology Development Organization (NEDO) revealed that the thermal
161 gradient of the conduction-dominated profile at N63-MS-6 (blue square in Figure 1c) was
162 170°C/km (New Energy and Industrial Technology Development Organization, 1990). This
163 thermal gradient suggests that temperatures can reach >400°C at a depth of 2.5 km. These
164 geophysical observations strongly indicate the possible existence of a supercritical geothermal
165 reservoir (>400°C) in this field.



166
 167 **Figure 1.** Maps of the study area. (a) Location of the Yuzawa geothermal field, NE Japan
 168 (orange star). (b) Regional map around the Yuzawa geothermal field. Dotted lines follow the
 169 outline of the calderas (Yoshida et al., 2014). Red triangles denote the major Quaternary
 170 volcanoes. (c) Local map of the Yuzawa geothermal field. White triangles denote MT sites. Blue
 171 circles denote hot springs. Magenta stars denote power plants (Uenotai: 28,500 kW and
 172 Wasabizawa: 46,200 kW). The red triangle denotes the Takamatsu volcano. The light blue
 173 square denotes the NEDO drilling site (N63-MS-6), reaching a depth of 1500 m (New Energy
 174 and Industrial Technology Development Organization, 1990).
 175

176 3. Methods

177 The MT method is a geophysical tool used to map the electrical resistivity structure of
 178 subsurfaces (Araya Vargas et al., 2019; Arnason et al., 2010; Becken et al., 2011; Bedrosian et
 179 al., 2018; Di Paolo et al., 2020; Heinson et al., 2018; Heise et al., 2008; Hyndman & Shearer,
 180 1989; Ichihara et al., 2016; Ingham et al., 2009; Le Pape et al., 2015; Moorkamp et al., 2019;
 181 Wise & Thiel, 2020). This method uses surface measurements of naturally occurring low-

182 frequency electromagnetic variations to infer subsurface resistivity structures (Chave & Jones,
 183 2012). Each MT station observes two electric field components (E_x and E_y) and three magnetic
 184 field components (H_x , H_y , and H_z). The x , y , and z directions are consistent with the geographic
 185 north, east, and vertical depths, respectively. The observed data were analyzed using the
 186 impedance tensor \mathbf{Z} and tipper \mathbf{T} , as follows:

$$\begin{bmatrix} E_x \\ E_y \\ H_z \end{bmatrix} = \begin{bmatrix} Z_{xx} & Z_{xy} \\ Z_{yx} & Z_{yy} \\ T_{zx} & T_{zy} \end{bmatrix} \begin{bmatrix} H_x \\ H_y \end{bmatrix}. \quad (1)$$

187 The complex impedance tensor in the frequency domain is expressed in terms of the apparent
 188 resistivity and phase for data interpretation (Chave & Jones, 2012). The complex impedance
 189 tensor is also expressed as a phase tensor since phase tensor is independent of the distorting
 190 effects produced by localized near-surface resistivity heterogeneities (Caldwell et al., 2004).

191 The observed MT data were converted into a surface-to-subsurface resistivity model using
 192 inversion analysis (Constable et al., 1987; Farquharson, 2008; Kelbert et al., 2014; Newman,
 193 2014; Ogawa & Uchida, 1996; Siripunvaraporn & Egbert, 2009). We used WSINV3DMT for the
 194 three-dimensional (3D) inversion of the observed MT data (Siripunvaraporn & Egbert, 2009).
 195 WSINV3DMT seeks to minimize the function as follows:

$$U = (\mathbf{m} - \mathbf{m}_0)^T \mathbf{C}_m^{-1} (\mathbf{m} - \mathbf{m}_0) + \lambda^{-1} \{ (\mathbf{d} - \mathbf{F}[\mathbf{m}])^T \mathbf{C}_d^{-1} (\mathbf{d} - \mathbf{F}[\mathbf{m}]) - \chi_*^2 \}, \quad (2)$$

196 where \mathbf{m} is the resistivity model, \mathbf{m}_0 is the prior model, \mathbf{d} is the observed data, $\mathbf{F}[\mathbf{m}]$ is the
 197 forward modeling response, \mathbf{C}_m is the model covariance, \mathbf{C}_d is a data covariance matrix, χ_* is the
 198 desired level of misfit, and λ^{-1} is a Lagrange multiplier. WSINV3DMT penalizes smoothed
 199 deviations from a prior model with spatial covariance. Thus, the obtained resistivity model by the
 200 regularized MT inversion is the smooth model away from a prior model.

201

202 4. Results

203 We collected MT data at 30 measurement sites to image resistivity structures in the Yuzawa
 204 geothermal field (Figure 1c). Since the objective of this study is to image supercritical
 205 geothermal reservoirs at depths of several kilometers, the MT site spacing is several kilometers.
 206 The phase tensor ellipses at 20 Hz showed higher phase values around Takamatsu volcano and
 207 power plants (Figure 2a). The phase tensor data suggest the existence of near-surface conductors.
 208 The phase tensor showed increased values at 2.5 Hz and decreased values at 0.3 Hz, which
 209 implies the presence of a deep conductor (Figure 2). The impedance and tipper data for each
 210 observation site are shown in Figure S1–S6.

211 Inverse modeling with WSINV3DMT converted the observed MT data into 3D resistivity
 212 structures (Siripunvaraporn et al., 2005; Siripunvaraporn & Egbert, 2009). The initial resistivity
 213 model for inverse modeling consisted of the subsurface (100 ohm-m), ocean (0.3 ohm-m), and
 214 air (10^{10} ohm-m). The prior resistivity model was set to be the same as the initial resistivity
 215 model. The computational grid consisted of $74 \times 74 \times 70$ cells, including boundary cells. In the
 216 central region of the model ($-10 \text{ km} < x$ and $y < 10 \text{ km}$), the mesh had a regular cell size of 300
 217 m in the horizontal direction. Outside this central region, the horizontal mesh size increased with
 218 increasing distance from the central region. For elevations between 1.3 km and 0 km, we set the
 219 vertical mesh size to values ranging from 20 m to 50 m. Note that elevation is indicated as height

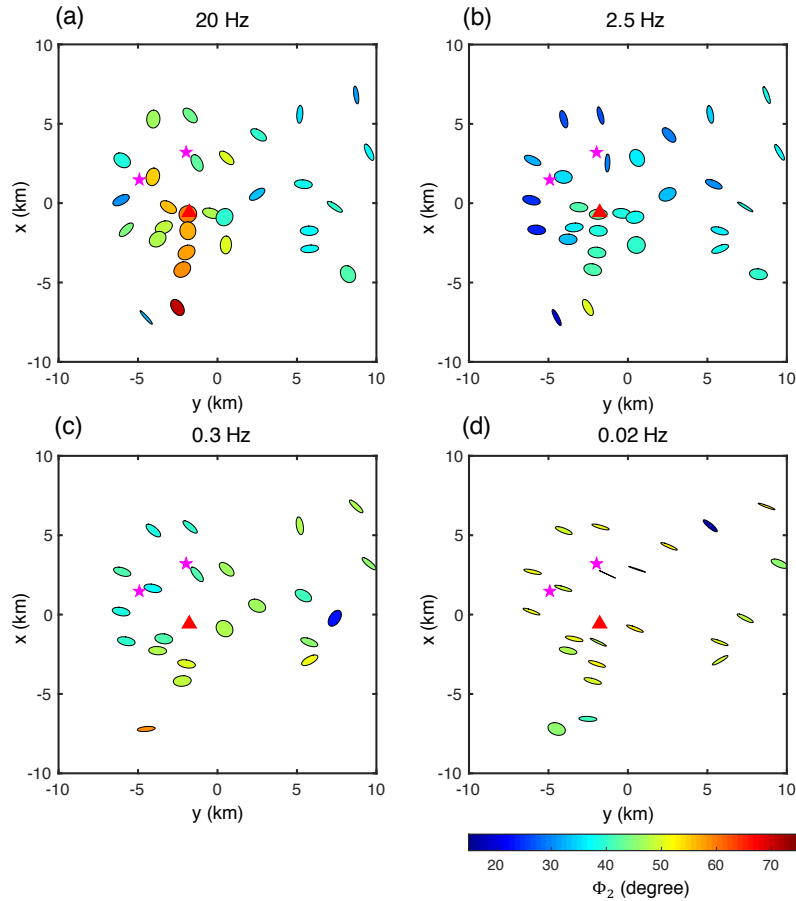
220 above sea level in this study. For elevations below 0 km, the mesh size increased with an
221 increasing depth. The computations of the inverse modeling were performed on a computer
222 (@Xeon 3.10 GHz Gold 6254 central processing unit; Intel Corp.) with 3 TB of RAM. The
223 impedance tensor and tipper between frequencies of 0.001–100 Hz (17 frequencies) were used
224 for inverse modeling. Error floors of 5% for the impedance tensor and 15% for the tipper were
225 used. The root-mean-square (RMS) misfit for the initial model was 10.2. The inversion analysis
226 obtained a resistivity model with an RMS misfit of 2.34 after three iterations (Figure 3). The data
227 fits were good for almost all sites and frequencies (Figure S1–S6).

228 3D resistivity structures obtained from the inverse modeling identified a near-surface conductor
229 at an elevation between 1.3 and –0.5 km, as well as a deep conductor C1 at an elevation between
230 –1.5 and –12 km (Figure 3). The resistivity of the near-surface conductor was 5–20 ohm-m,
231 which was lower than that of the surrounding rock of 100 ohm-m. Near-surface conductors were
232 widely distributed in this area. The resistivity value of C1 was approximately 10 ohm-m. These
233 low resistivity anomalies are consistent with the features of the observed data (Figure 2 and
234 Figure S1–S6). C1 was imaged northeast of Takamatsu volcano and not immediately below the
235 volcano. The size of C1 was 3 km (width) \times 5 km (length) \times 10 km (height). Conductive zones
236 extended from the east and west ends of deep conductor C1 to the near-surface conductors
237 (Figure 3c). The conductor zone extending from the west end of C1 extended towards the
238 Wasabizawa power plant (Figure 3c). Although a deep conductor was imaged at $y = 9$ km
239 outside the coverage area of the receiver (Figure 3c), the MT data did not sufficiently constrain
240 resistivity structures outside the coverage area of the receiver. Therefore, we have excluded this
241 conductor from our discussions in this study.

242 The deep conductor C1 is potentially related to a supercritical fluid reservoir. It is known that the
243 MT method is uncertain, especially for deep resistivity structures, such as C1 (Ishizu et al., 2021).
244 We calculated the MT responses for models where the resistivity value of C1 was replaced by 1–
245 100 ohm-m to determine how well this resistivity value was constrained by the data (Figure S7).
246 The RMS misfit was minimum for 10 ohm-m and increased away from 10 ohm-m (Figure S7).
247 Reliability was measured based on F values with a 95% confidence interval (Gresse et al., 2021;
248 Yamaya et al., 2017). The threshold RMS misfit with a 95% confidence interval was 2.392.
249 Forward models associated with C1: $6.5 \text{ ohm-m} < C1 < 35 \text{ ohm-m}$ obtained a RMS misfit
250 < 2.392 . Forward models associated with low and high resistivities (i.e. $< 6.5 \text{ ohm-m}$ and > 35
251 ohm-m) showed RMS values higher than $F_{\text{RMS}} = 2.392$. In other words, these forward models
252 were statistically rejected with a 95% confidence interval. Hence, we conclude that the resistivity
253 range of C1 is $6.5 \text{ ohm-m} < C1 < 35 \text{ ohm-m}$.

254

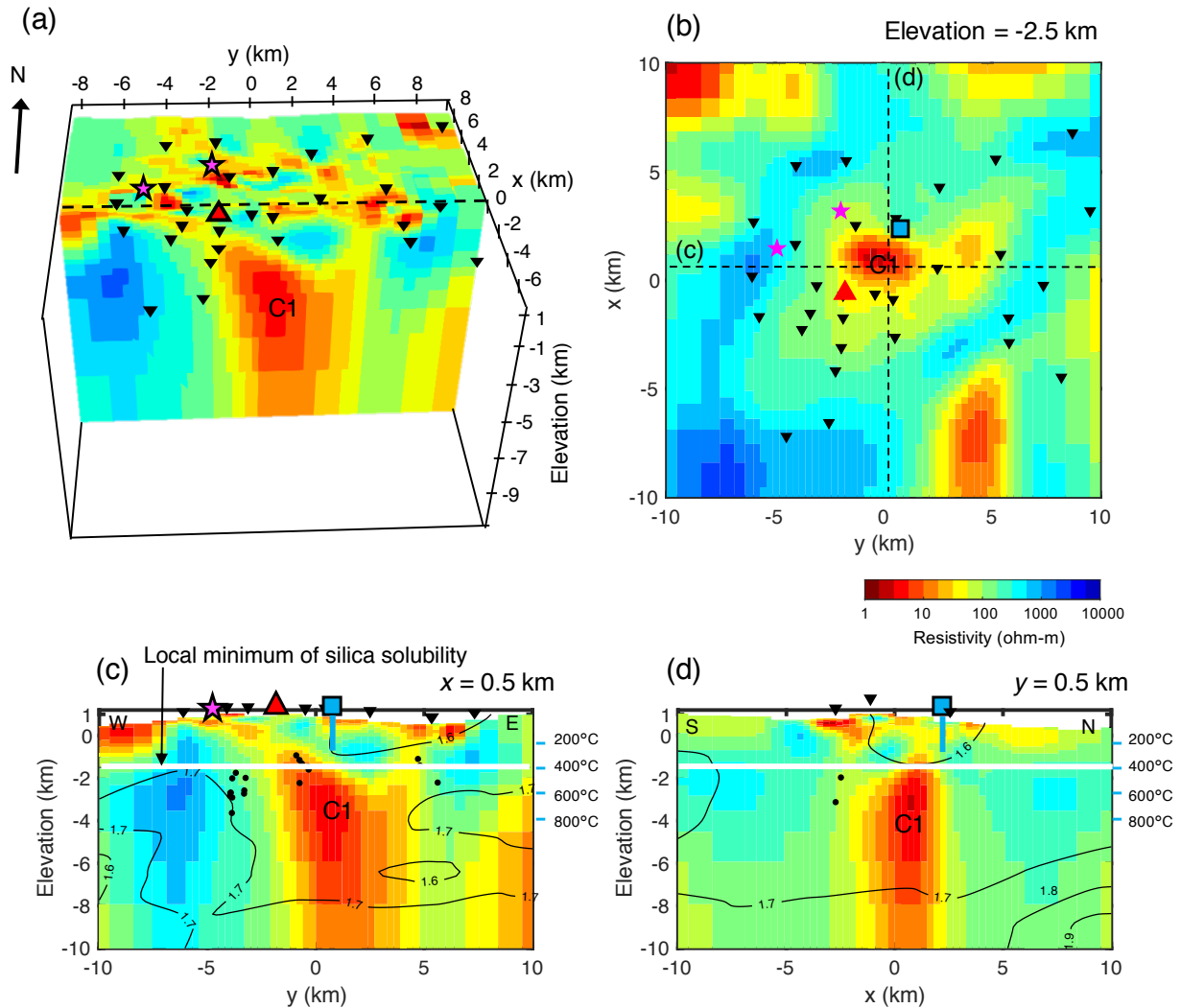
255



256

257 **Figure 2.** Phase tensor ellipses of observed MT data for (a) 20 Hz, (b) 2.5 Hz, (c) 0.3 Hz, and
 258 0.02 Hz. The phase tensor ellipses are filled by $\tan^{-1}(\Phi_2)$, where Φ_2 is the geometric mean of the
 259 diagonal components of the phase tensor components (Φ_{max} and Φ_{min}) (Caldwell et al., 2004).
 260 Phase tensor ellipses have been normalized by the maximum phase value. Magenta stars denote
 261 power plants. The red triangle denotes Takamatsu volcano. Note that x and y directions are
 262 consistent with the geographic north and east, respectively.

263



264
 265 **Figure 3.** (a) 3D view with vertical slice at $x = 0.5$ km; (b) horizontal slice at an elevation of -2.5
 266 km; (c) vertical slice at $x = 0.5$ km; (d) vertical slice at $y = 0.5$ km of the inverted resistivity
 267 model from the MT data. C1 denotes conductive zones, which imply a supercritical fluid and
 268 partial melting. Black triangles denote MT sites. Magenta stars denote power plants. The red
 269 triangle denotes Takamatsu volcano. The light blue square denotes the NEDO drilling sites
 270 (N63-MS-6). Contours of V_p/V_s ratio (Okada et al., 2014) are superimposed on the sections in
 271 (c) and (d). Black triangles denote MT sites within ± 1 km of each profile line. Black dots denote
 272 the relocated hypocenters of earthquakes within ± 150 m of each profile line (Okada et al., 2014).
 273 White lines denote the depth of a local minimum of silica solubility, as presented in Figure 5.
 274 Note that elevation is indicated as height above sea level, and x and y directions denote the
 275 geographic north and east, respectively.
 276

277 **5. Discussion**278 **5.1 Shallow hydrothermal system**

279 Initially, a shallow geothermal system was investigated using the obtained resistivity model. The
280 resistivity model revealed the near-surface conductor at an elevation greater than -0.5 km
281 (Figure 3). Similar near-surface conductors found in various volcanic areas have been interpreted
282 as smectite-rich zones (Cherkose & Saibi, 2021; Kanda et al., 2019; Ledo et al., 2021; Tseng et
283 al., 2020; Yoshimura et al., 2018). Drilling confirmed the smectite-rich zones in this field (New
284 Energy and Industrial Technology Development Organization, 1990). Moreover, the distribution
285 of near-surface conductors was consistent with the distribution of hydrothermal alteration zones
286 on the surface (Nunohara et al., 2021). These results indicate that the near-surface conductor was
287 a smectite-rich zone. Furthermore, the bottom of the near-surface conductors was roughly
288 consistent with the isotherm at 200°C (Figure 3d). Smectite under moisture-rich conditions can
289 be converted to illite at temperatures exceeding 200°C (Wersin et al., 2007; Yamaya et al., 2013).
290 The resistivity of illite was much higher than that of smectite (Ussher et al., 2000). Hence, we
291 interpreted the resistive zone below the near-surface conductors as an illite-rich zone transformed
292 from smectite above 200°C .

293 Conductive zones were found to extend from the east and west ends of deep conductor C1 to the
294 near-surface conductors (Figure 3c). The conductor zone extending from the west end of C1
295 extended towards the Wasabizawa power plant (Figure 3c). The $^3\text{He}/^4\text{He}$ and $^4\text{He}/^{20}\text{Ne}$ ratios of
296 the fumarolic gas at the Kawarage hot spring, located 3 km west of the Wasabizawa power plant,
297 were 9.5×10^{-6} and 180, respectively (Kita et al., 1992). This indicates that the helium at the
298 Kawarage hot spring originated from magmatic gas. These results suggest that these conductive
299 zones act as a path for magmatic fluid ascending from C1, resulting in anomalies in the helium
300 ratios at the Kawarage hot spring. A conductor extending from the deep parts (25 km depth) to
301 the surface at Naruko volcano also represented a path for ascending magmatic fluid (Ogawa et al.,
302 2014).

303 **5.2 Supercritical geothermal reservoir**

304 The low resistivity of C1 suggests that it includes fluids (magmatic fluids and melts). The
305 geometry of C1 is consistent with low V_p and V_s zones, supporting that C1 contains magmatic
306 fluids and melts (Figure S8). The temperature of C1 was estimated to be above 400°C based on
307 the temperature profile (Figure 4a). While a few seismicities occurred inside C1, most occurred
308 around the edge of C1 (Figure 3). The depth of the seismicity cut-off was consistent with that of
309 C1, and it is known that the depth of the seismicity cut-off roughly corresponds to 400°C
310 (Mitsuhashi et al., 2001; Ogawa et al., 2001; Okada et al., 2014). The correspondence between the
311 top of C1 and the seismicity cut-off also supports that C1 was $>400^{\circ}\text{C}$.

312 Similar conductors at depths of 2–15 km in other volcanoes have been interpreted as magmatic
313 fluids and melts depending on the temperature and pressure (e.g., Mount St Helens: Bedrosian et
314 al., 2018, Geysers: Peacock et al., 2020, Laguna del Maule: Cordell et al., 2020, Kirishima:
315 Aizawa et al., 2014; Taupo: Bertrand et al., 2012, Krafla: Lee et al., 2020). A minimum solidus
316 temperature of 725°C at a pressure of 100 MPa (Bowles-Martinez & Schultz, 2020; Tuttle &
317 Bowen, 1958), suggested that the part of C1 at a temperature lower than 725°C was comprised of
318 magmatic fluid. The thermal gradient of $170^{\circ}\text{C}/\text{km}$ suggests that the temperature at an elevation
319 of -4 km becomes 725°C (Figure 4a). Therefore, we considered the upper part of C1 at an

320 elevation greater than -4 km as a potential supercritical fluid reservoir ($>400^{\circ}\text{C}$) instead of melt.
321 The low V_p/V_s ratio (<1.7) in the upper parts of C1 (Figure 3 and Figure S8) also indicated that
322 the upper parts were mainly magmatic fluid instead of melt (Okada et al., 2014).

323 NaCl-H₂O fluids can be found in different phases depending on the pressure, temperature, and
324 salinity conditions (Afanasyev et al., 2018; Driesner & Heinrich, 2007; Sillitoe, 2010; Weis et al.,
325 2012). Three fluid phases (1: single-phase, 2: vapor-liquid coexisting phase, 3: vapor-halite
326 coexisting phase) can be expected for supercritical fluids (Figure 5a). The fluid phase can affect
327 the resistivity of the NaCl-H₂O fluids. The typical NaCl content of magmatic fluids is 5–10 wt%,
328 based on fluid inclusion analysis (Heinrich, 2005). Recent mantle xenolith studies reported the
329 NaCl content of fluids in the mantle wedge to be 5.1 wt% (Kawamoto et al., 2013). First, we
330 consider that the magmatic fluid has a 5 wt% NaCl equivalent. The pressure at the potential
331 supercritical reservoir is expected to be hydrostatic or lithostatic, or somewhere between the two
332 (Figure 4b). We calculated the hydrostatic pressure assuming a water density of 1000 kg/m^3 and
333 lithostatic pressure assuming a rock density of 2700 kg/m^3 (Saishu et al., 2014).

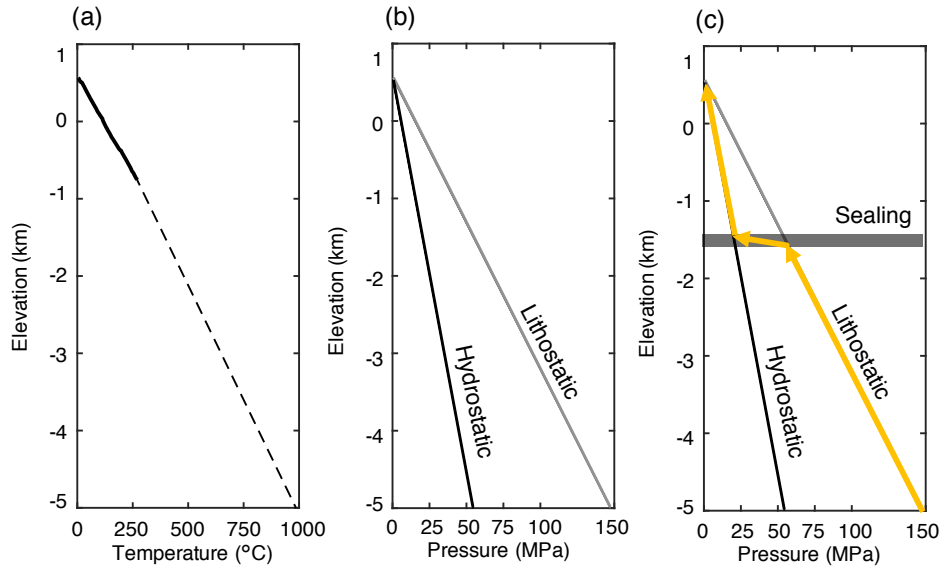
334 We consider the fluid phase of the reservoir top at an elevation of -1.8 km (temperature of
335 450°C) because shallow parts are easier to exploit than deeper parts. The phase of the
336 supercritical fluid is a vapor-halite coexisting phase at 450°C if the pressure is in the hydrostatic
337 condition (Figure 5a). We assumed that the halite is resistive at $>10^8$ ohm-m (Watanabe & Peach,
338 2002), while the vapor is resistive at 1000 ohm-m (Peacock et al., 2020). As a result, the vapor-
339 halite coexisting phase is estimated to be much more resistive than the 10 ohm-m of C1. The
340 phase of the supercritical fluid is a vapor-liquid coexisting phase at 450°C if the pressure is
341 below the average between hydrostatic and lithostatic conditions (e.g. 35 MPa) (Figure 5a). In
342 the vapor-liquid coexisting phase, the fluid exists as low-salinity vapor in equilibrium with a
343 small fraction of hypersaline brine (Driesner & Heinrich, 2007). Despite a lack of laboratory
344 measurement data for the resistivity of the vapor-liquid coexisting phase, to the best of our
345 knowledge, the two-phase zones have been reported as resistive zones of 100 – 1000 ohm-m
346 (Gresse et al., 2021; Samrock et al., 2018), which are much more resistive than 10 ohm-m of C1.
347 The phase of the supercritical fluid is single-phase at 450°C if the pressure is in the lithostatic
348 condition (Figure 5a). Bannard (1975) showed that the resistivity of a single phase is low. If we
349 consider a single-phase supercritical fluid under pressure close to the lithostatic pressure, 10
350 ohm-m can be reasonably explained. Therefore, the supercritical fluid was considered as a
351 single-phase fluid under pressure close to the lithostatic pressure. Although the magmatic fluid
352 was considered to have a 5 wt% NaCl equivalent, a higher pressure close to the lithostatic
353 pressure was also predicted for the magmatic fluid with 10 wt% NaCl equivalent to a single-
354 phase (Figure 5b).

355 If a connection exists to the surface from the supercritical fluid reservoir, the pressure should be
356 under hydrostatic conditions in the supercritical fluid reservoir. Hence, sealing to weaken the
357 connections should be considered as an explanation for the lithostatic pressure of the reservoir
358 (Scholz, 2019; Sibson, 2020). Silica sealing has been found above the potential supercritical
359 reservoir and may separate the hydrostatic and lithostatic regions (Fournier, 1999; Ingebritsen &
360 Manning, 2010; Lowell et al., 1993; Manning, 1994; Saishu et al., 2014; Weatherley & Henley,
361 2013). To consider the potential of silica sealing in this field, we calculated the silica solubility
362 using Loner AP software (Akinfiev & Diamond, 2009). The quartz solubility had a local
363 minimum for hydrostatic pressure, indicating that quartz precipitation could occur at this depth
364 from downward-moving fluids (surface to deep) (Figure 6). The depth of the local minimum was

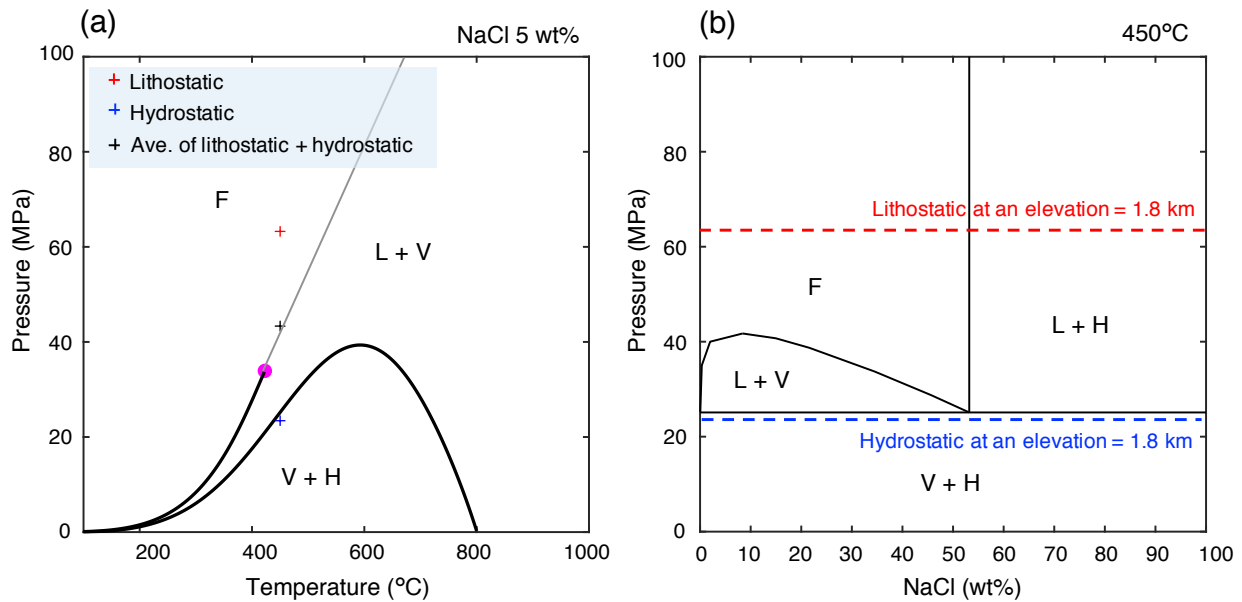
365 consistent with that of the top of C1. This suggests that silica sealing exists above C1. After the
366 development of silica sealing by downward-moving fluids with hydrostatic pressure, the
367 developed silica sealing weakens the connection from the supercritical fluid reservoir to the
368 surface. Moreover, upward-moving fluids with lithostatic pressure from the deep parts of the
369 crust can enhance the sealing if the upward-moving fluid encounters the fluids with hydrostatic
370 pressure due to differences in their silica solubility (Fournier, 1999; Saishu et al., 2014). These
371 mechanisms can explain why the silica sealing developed there and separate the hydrostatic and
372 lithostatic regions (Figure 4c). The silica sealing also plays a role in trapping the upwelling
373 supercritical fluids due to its low permeability.

374 We considered the fluid fraction of a potential supercritical reservoir using the obtained
375 resistivity model. We assumed that the potential supercritical reservoir is comprised of a
376 complex (supercritical fluid and solid phase). The bulk resistivity of the potential supercritical
377 reservoir was modeled using the Hashin–Shtrikman upper bound model (HS+) (Hashin &
378 Shtrikman, 1962). We used the resistivity values of NaCl-H₂O fluids reported by Bannard (1975)
379 for the resistivity of supercritical fluid. The solid-phase resistivity was fixed at 1000 ohm-m.
380 Reservoir pressure was assumed to be under the lithostatic condition (Figure 4c). For the C1 top
381 at an elevation of -1.8 km (450°C and 60 MPa), 10 ohm-m resistivity of C1 required a fluid
382 fraction of 1% and 0.5% for 5 wt% and 10 wt% NaCl equivalent, respectively (Figure 7). Ishizu
383 et al. (2021) found that MT inversion often overestimates the resistivity of deep conductors by
384 modeling studies (i.e. the estimated resistivity is higher than the true resistivity). Thus, the true
385 resistivity of C1 is expected to be lower than 10 ohm-m. If we consider the lower bound *F* value
386 (6.5 ohm-m), the fluid fractions are 2% and 1% for 5 wt% and 10 wt% NaCl equivalent,
387 respectively (Figure 7). The 0.5–2% fluid fraction of the potential supercritical fluids estimated
388 by the resistivity model was consistent with the porosity (1.7%) of the core sample of the
389 Kakkonda granite near the bottom of the WD-1a well (Muraoka et al., 1998). The resistivity of
390 supercritical fluids depends on the temperature and pressure (Bannard, 1975; Nono et al., 2020).
391 Although measurement data of the resistivity values of NaCl-H₂O fluids at higher temperatures
392 and pressures (e.g. 600°C and 100 MPa) is lacking, the resistivity was predicted to be higher than
393 that at 450°C and 60 MPa, according to the measurements reported by Bannard (1975). This
394 indicates that a fluid fraction higher than 0.5–2% is predicted for the bottom of the reservoir.
395 However, the bottom of the supercritical reservoir is not currently economically exploitable
396 because of the low permeability and high cost of deep drilling (Watanabe et al., 2017).

397

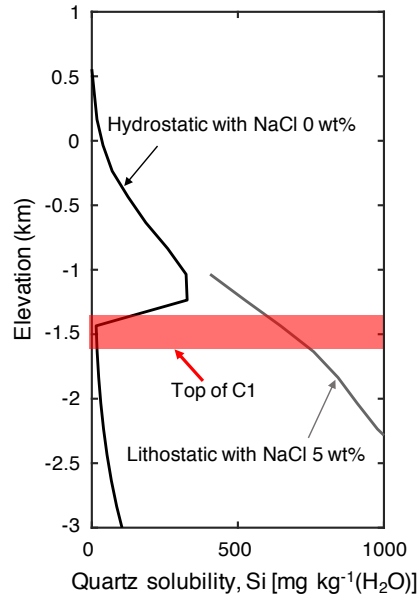


398
 399 **Figure 4.** (a) Temperature profile as a function of elevation at the NEDO drilling sites (N63-MS-
 400 6), as presented in Figure 1b (New Energy and Industrial Technology Development Organization,
 401 1990). The solid line denotes logging data and the dashed line denotes the extrapolated profile.
 402 (b) The pressure profile as a function of elevation under hydrostatic pressure (black line) and
 403 lithostatic pressure (grey line), respectively. We calculated the hydrostatic pressure assuming a
 404 water density of 1000 kg/m^3 and lithostatic pressure assuming a rock density of 2700 kg/m^3
 405 (Saishu et al., 2014).
 406



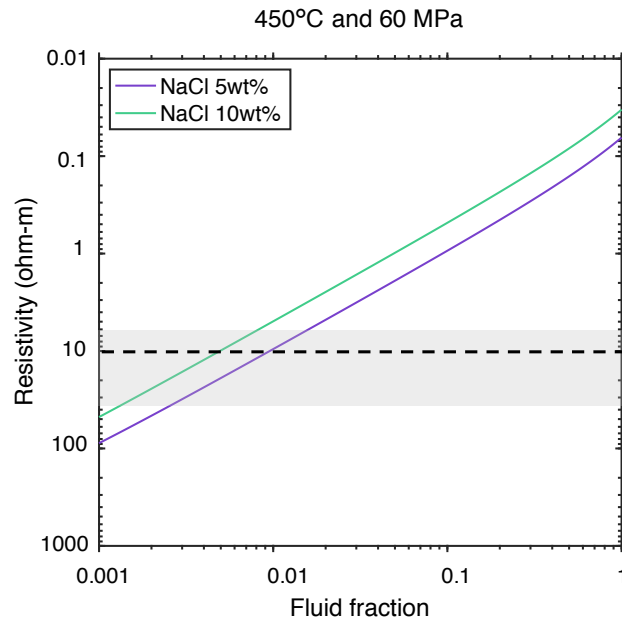
407
 408 **Figure 5.** (a) Pressure-temperature diagram of NaCl-H₂O solution for 5 wt% NaCl equivalent,
 409 calculated using AqSo_NaCl software (Bakker, 2018). The magenta circle denotes the critical
 410 point (422°C and 34 MPa). Red, blue, and black crosses denote the pressure-temperature points
 411 at an elevation of -1.8 km (450°C) under lithostatic, hydrostatic, and average of lithostatic and
 412 hydrostatic, respectively. (b) Isothermal pressure-composition sections for 450°C. The red and

413 blue lines denote pressure at an elevation of -1.8 km under hydrostatic and lithostatic conditions.
 414 L, liquid, V, vapor, H, halite; for temperatures equal to or higher than the critical temperature of
 415 the fluid, the notation F, fluid was introduced to underline that those fluid properties can
 416 gradually change from liquid-like to vapor-like without crossing a phase boundary in this region
 417 (Driesner & Heinrich, 2007).
 418



419
 420 **Figure 6.** Quartz solubility profiles as a function of depth, calculated using Loner AP software
 421 (Akinfiyev & Diamond, 2009). The solubility for pure H_2O under hydrostatic conditions (salinity
 422 = 0 wt%; black line) and the solubility for saline fluid under lithostatic conditions (5 wt% NaCl
 423 equivalent; grey line) are shown. The red dashed line denotes the top of C1, as shown in Figure 3.

424



425

426 **Figure 7.** The bulk resistivity of the complex (supercritical fluid and solid phase) at 450°C and
 427 60 MPa as a function of fluid fraction and of NaCl content in the supercritical fluid. Supercritical
 428 fluid resistivity was calculated based on the laboratory measurement results of Bannard (1975).
 429 Bulk resistivity was calculated using Hashin–Shtrikman upper bound model (*HS+*) (Hashin &
 430 Shtrikman, 1962). Solid phase resistivity was fixed at 1000 ohm-m. The gray zone denotes the
 431 resistivity range with a 95% confidence interval for C1 based on *F*-test ($6.5 \text{ ohm-m} < C1 < 35$
 432 ohm-m).
 433

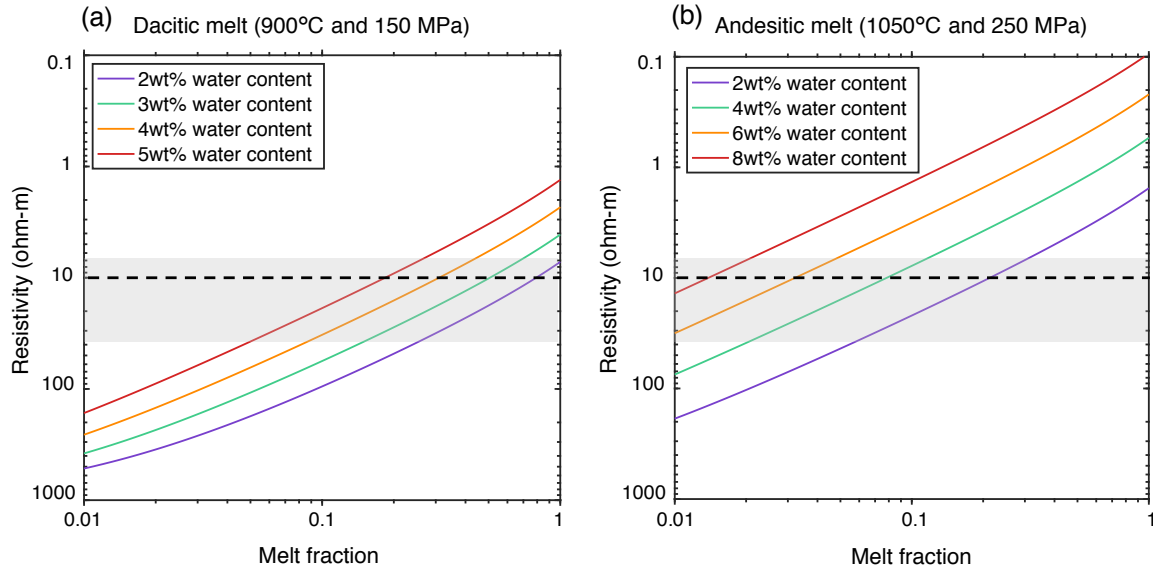
434 5.3. Partial melt

435 The temperature at an elevation lower than -5 km was estimated to be above 800°C . This
 436 temperature of 800°C was over the minimum solidus temperature of 725°C at a pressure of 100
 437 MPa for silicic melts (Bowles-Martinez & Schultz, 2020; Tuttle & Bowen, 1958). Therefore, C1
 438 may include a melt at an elevation lower than -5 km . Resistivity models are useful for inferring
 439 the melt fraction in the subsurface (Feucht et al., 2017; Hata et al., 2015; Hill et al., 2009; Ichiki
 440 et al., 2021; Lee et al., 2020; Peacock et al., 2015; Piña-Varas et al., 2018; Samrock et al., 2018).
 441 The resistivity of the melt has been well studied in the literature (Gaillard & Marziano, 2005;
 442 Guo et al., 2017; Laumonier et al., 2015; Pommier & Le-Trong, 2011). Here, we assume that the
 443 part of C1 with a temperature above 800°C consists of a complex (melt and solid phase).

444 A petrologic study revealed that dacitic and andesitic melts are likely to exist in this field (Ban et
 445 al., 2007). The dacitic melt has a shallower origin than the andesitic melt (Ban et al., 2007;
 446 Tatsumi et al., 2008). We assume that conductor C1 at an elevation of -5 km consists of the
 447 complex (dacitic melt and solid phase), and used the resistivity value reported by Laumonier et al.
 448 (2015) for dacitic melt. Bulk resistivity was calculated using the Hashin–Shtrikman upper bound
 449 model (*HS+*) (Hashin & Shtrikman, 1962) The solid-phase resistivity was fixed at 1000 ohm-m.
 450 The bulk resistivity of the complex (dacitic melt and solid phase) at 900°C and 150 MPa (-5 km
 451 elevation) suggests that an 80% melt fraction with 2 wt% H_2O is required to explain the 10 ohm-
 452 m of C1. As mentioned above, the MT method may overestimate the resistivity values (Ishizu et
 453 al., 2021). If we consider the lower bound of C1 (6.5 ohm-m), the 100% melt fraction is
 454 considered for 2 wt% H_2O . However, these melt fractions are not reasonable. The water content
 455 in the dacitic melt can range up to 5.5 wt%, which is the water saturation condition (Wallace,
 456 2005). If the dacitic melt was almost water-saturated (5 wt% H_2O), the 20% melt fraction could
 457 explain 10 ohm-m. Even if we consider the lower bound of C1 (6.5 ohm-m), the 30% melt
 458 fraction was considered for 5 wt% H_2O . These findings suggest that C1 at an elevation of -5 km
 459 is a dacitic melt with 5 wt% H_2O and a melt fraction of 20–30%.

460 The andesitic melt is expected to be located in the deep zones of this field (Ban et al., 2007). The
 461 conductor C1 at an elevation of -9 km was assumed to consist of a complex (andesitic melt and
 462 solid phase). The resistivity of the andesitic melt was calculated according to Guo et al. (2017).
 463 To explain 10 ohm-m of C1 at 1050°C and 250 MPa (-9 km elevation), the melt fraction was
 464 estimated to be 2% for 8 wt% H_2O and 20% for 2 wt% H_2O . Hence, our resistivity model
 465 suggests that C1 at an elevation of -9 km consists of an andesitic melt with a melt fraction below
 466 20%.

467



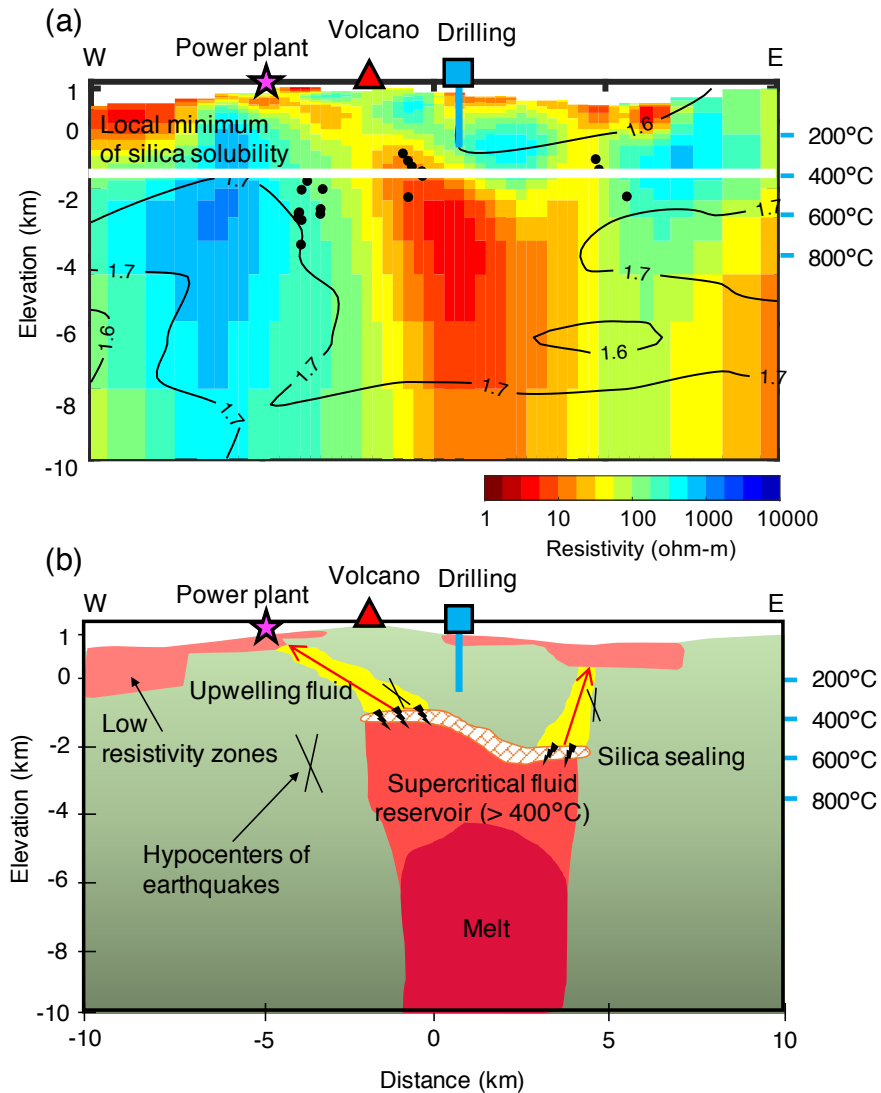
468
 469 **Figure 8.** (a) The bulk resistivity of the complex (dacitic melt and solid phase) at 900°C and 150
 470 MPa as a function of melt fraction and water content in the dacitic melt. The resistivity of the
 471 dacitic melt was calculated based on Laumonier et al. (2015). Solid phase resistivity was fixed at
 472 1000 ohm-m. Bulk resistivity was calculated using Hashin–Shtrikman upper bound model (HS+).
 473 (b) The bulk resistivity of the complex (andesitic melt and solid phase) at 1050°C and 250 MPa
 474 as a function of melt fraction and water content in the andesitic melt. The resistivity of the
 475 andesitic melt was calculated based on Guo et al. (2017). The gray zones denote the resistivity
 476 range with a 95% confidence interval for C1 based on the F -test ($6.5 \text{ ohm-m} < C1 < 35 \text{ ohm-m}$).
 477

478 5.4. Mechanism of evolution of a supercritical geothermal reservoir

479 Our MT data revealed a potential supercritical geothermal reservoir, a melt, and a shallow
 480 geothermal system in the Yuzawa geothermal field in NE Japan (Figure 3). Based on our
 481 resistivity model, we propose a mechanism for the evolution of a supercritical geothermal
 482 reservoir (Figure 9). The dacitic and andesitic melt below the supercritical geothermal reservoir
 483 may supply magmatic fluids to the supercritical geothermal reservoir (Blundy et al., 2021;
 484 Heinrich, 2005; Sillitoe, 2010). Upwelling supercritical fluids supplied from the melt were found
 485 to become trapped under a less-permeable silica sealing, and supercritical fluids accumulated
 486 below the silica sealing as a result (Figure 9). Silica sealing separates the hydrostatic and
 487 lithostatic regions (Figure 4c). Hence, the supercritical geothermal reservoir below the silica
 488 sealing is under lithostatic pressure, and the phase of the potential supercritical fluids is
 489 interpreted as a single phase. Single-phase supercritical fluids show low resistivity (Bannard,
 490 1975). Therefore, the supercritical fluid reservoir was imaged as a low resistivity anomaly of C1
 491 (Figure 3). The fluid fraction of the supercritical reservoir was estimated to be 0.5–2% (Figure 7).
 492 Episodic supplies of magmatic fluids from the melt increased the pressure of the supercritical
 493 fluid reservoir, with high levels of pressure subsequently breaking the silica sealing. Fluids
 494 leaking from the silica sealing moved to the surface (Figure 9). The fluids were detected as
 495 conductive zones extending from the deep conductor C1 to the near-surface conductors (Figure
 496 3c). The smectite-rich zones near the surface act as an impermeable cap-to-trap hydrothermal
 497 fluid of mixed meteoric water and upwelling fluids owing to its low permeability (Revil et al.,

498 2019). Power plants in operation in the area use hydrothermal fluids (<300°C) trapped below the
 499 impermeable cap of smectite to generate electric energy (New Energy and Industrial Technology
 500 Development Organization, 1990). Since our MT data revealed a potential supercritical
 501 geothermal reservoir in this geothermal field, power plants in this field potentially may use
 502 supercritical geothermal reservoirs to increase their power generation in the future.

503



504 **Figure 9.** (a) West–east cross-section at $x = 0.5$ km of the inverted resistivity model. This cross-
 505 section is the same as Figure 3c. Symbols are the same as in Figure 3. (b) Schematic model of a
 506 geothermal system inferred from our resistivity model.
 507
 508

509 **6. Conclusions**

510 Supercritical geothermal reservoirs are next-generation energy resources that yield higher
 511 productivity than conventional geothermal fluids with temperatures <350°C. Despite the fact that
 512 understanding the fluid fraction and spatial distribution of supercritical geothermal reservoirs is

513 necessary for their assessment as a energy resource, these characteristics remain poorly
514 understood. Therefore, to gain insights into the fluid fraction and spatial distribution of a
515 supercritical geothermal reservoir, we applied the MT method in the Yuzawa geothermal field in
516 NE Japan. As a result, this study is the first to present a detailed estimation of the spatial
517 distribution and fluid fraction of a potential supercritical geothermal reservoir. Our main findings
518 can be summarized as follows:

- 519 • The MT data revealed a supercritical geothermal reservoir, a melt, and a shallow
520 geothermal system in the Yuzawa geothermal field.
- 521 • The MT data revealed a supercritical geothermal reservoir (>400°C) with a size of 3 km
522 (width) × 5 km (length) at a depth of 2.5–6 km. The fluid fraction of the supercritical
523 reservoir was estimated to be 0.5–2% with a salinity of 5–10 wt%.
- 524 • Silica sealing may exist above the potential supercritical geothermal reservoir, separating
525 the hydrostatic and lithostatic regions. The potential supercritical fluids were considered
526 to be under lithostatic pressure, and the fluid phase was interpreted as being single-phase.
- 527 • The MT data indicate that dacitic and andesitic melts exist below the supercritical fluid
528 reservoir. The melt supplies magmatic fluid to the supercritical fluid reservoir.
- 529 • We propose a mechanism for the evolution of a supercritical fluid reservoir, wherein
530 upwelling supercritical fluids supplied by the melt are trapped under less permeable silica
531 sealing. As a result, supercritical fluids accumulate below the silica sealing.
- 532 • The supercritical fluid breaking from the silica sealing provides upward-moving fluids to
533 the surface.

535 **Acknowledgments**

536 This work was supported by the Japan Society for the Promotion of Science KAKENHI
537 (20K22326 and 21109003). We thank Prof. Weerachai Siripunvaraporn for allowing us to use
538 the 3D MT inversion code and Prof. Tomomi Okada for providing seismic data and velocity
539 models. We are grateful to Dr. Norihiro Watanabe for helpful discussions on the resistivity of
540 supercritical fluids and Dr. Ryoichi Yamada for his help with the geological interpretation of the
541 resistivity model.

543 **Data Availability Statement**

544 Data archiving is in progress, and the MT data used in this study will be available from the
545 SPUD EMTF repository by the time this paper is accepted for publication. For the period of peer
546 review, the MT data can be obtained from Supporting Information.

548 **References**

- 549 Afanasyev, A., Blundy, J., Melnik, O., & Sparks, S. (2018). Formation of magmatic brine lenses
550 via focussed fluid-flow beneath volcanoes. *Earth and Planetary Science Letters*, *486*, 119–
551 128. <https://doi.org/10.1016/j.epsl.2018.01.013>
- 552 Aizawa, K., Koyama, T., Hase, H., Uyeshima, M., Kanda, W., Utsugi, M., et al. (2014). Three-

- 553 dimensional resistivity structure and magma plumbing system of the Kirishima Volcanoes as
 554 inferred from broadband magnetotelluric data. *Journal of Geophysical Research: Solid Earth*,
 555 *119*(1), 198–215. <https://doi.org/10.1002/2013JB010682>
- 556 Akinfiyev, N. N., & Diamond, L. W. (2009). A simple predictive model of quartz solubility in
 557 water–salt–CO₂ systems at temperatures up to 1000°C and pressures up to 1000MPa.
 558 *Geochimica et Cosmochimica Acta*, *73*(6), 1597–1608.
 559 <https://doi.org/10.1016/j.gca.2008.12.011>
- 560 Araya Vargas, J., Meqbel, N. M., Ritter, O., Brasse, H., Weckmann, U., Yáñez, G., & Godoy, B.
 561 (2019). Fluid distribution in the Central Andes subduction zone imaged with magnetotellurics.
 562 *Journal of Geophysical Research: Solid Earth*, *124*(4), 4017–4034.
 563 <https://doi.org/10.1029/2018JB016933>
- 564 Árnason, K., Eysteinnsson, H., & Hersir, G. P. (2010). Joint 1D inversion of TEM and MT data and
 565 3D inversion of MT data in the Hengill area, SW Iceland. *Geothermics*, *39*(1), 13–34.
 566 <https://doi.org/10.1016/j.geothermics.2010.01.002>
- 567 Bakker, R. J. (2018). AqSo_NaCl: Computer program to calculate p-T-V-x properties in the H₂O-
 568 NaCl fluid system applied to fluid inclusion research and pore fluid calculation. *Computers &*
 569 *Geosciences*, *115*, 122–133. <https://doi.org/10.1016/j.cageo.2018.03.003>
- 570 Bali, E., Aradi, L. E., Zierenberg, R., Diamond, L. W., Pettke, T., Szabó, Á., et al. (2020).
 571 Geothermal energy and ore-forming potential of 600 °C mid-ocean-ridge hydrothermal fluids.
 572 *Geology*, *48*(12), 1221–1225. <https://doi.org/10.1130/G47791.1>
- 573 Ban, M., Hirotsu, S., Wako, A., Suga, T., Iai, Y., Kagashima, S., et al. (2007). Origin of felsic
 574 magmas in a large-caldera-related stratovolcano in the central part of NE Japan —
 575 Petrogenesis of the Takamatsu volcano. *Journal of Volcanology and Geothermal Research*,
 576 *167*(1), 100–118. <https://doi.org/10.1016/j.jvolgeores.2007.05.008>
- 577 Bannard, J. E. (1975). Effect of density on the electrical conductance of aqueous sodium chloride
 578 solutions. *Journal of Applied Electrochemistry*, *5*(1), 43–53.
 579 <https://doi.org/10.1007/BF00625958>
- 580 Becken, M., Ritter, O., Bedrosian, P. A., & Weckmann, U. (2011). Correlation between deep fluids,
 581 tremor and creep along the central San Andreas fault. *Nature*, *480*(7375), 87–90.
 582 <https://doi.org/10.1038/nature10609>
- 583 Bedrosian, P. A., Peacock, J. R., Bowles-Martinez, E., Schultz, A., & Hill, G. J. (2018). Crustal
 584 inheritance and a top-down control on arc magmatism at Mount St Helens. *Nature Geoscience*,
 585 *11*(11), 865–870. <https://doi.org/10.1038/s41561-018-0217-2>
- 586 Bertrand, E. A., Caldwell, T. G., Hill, G. J., Wallin, E. L., Bennie, S. L., Cozens, N., et al. (2012).
 587 Magnetotelluric imaging of upper-crustal convection plumes beneath the Taupo Volcanic
 588 Zone, New Zealand. *Geophysical Research Letters*, *39*(2).
 589 <https://doi.org/10.1029/2011GL050177>
- 590 Blundy, J., Afanasyev, A., Tattitch, B., Sparks, S., Melnik, O., Utkin, I., & Rust, A. (2021). The
 591 economic potential of metalliferous sub-volcanic brines. *Royal Society Open Science*, *8*(6),
 592 202192. <https://doi.org/10.1098/rsos.202192>
- 593 Bowles-Martinez, E., & Schultz, A. (2020). Composition of magma and characteristics of the
 594 hydrothermal system of Newberry volcano, Oregon, from Magnetotellurics. *Geochemistry*,
 595 *Geophysics, Geosystems*, *21*(3), e2019GC008831. <https://doi.org/10.1029/2019GC008831>
- 596 Caldwell, T. G., Bibby, H. M., & Brown, C. (2004). The magnetotelluric phase tensor.
 597 *Geophysical Journal International*, *158*(2), 457–469. <https://doi.org/10.1111/j.1365-246X.2004.02281.x>

- 599 Chave, A. D., & Jones, A. G. (2012). Introduction to the magnetotelluric method. In *The*
600 *Magnetotelluric Method: Theory and Practice* (p. 570). Cambridge: Cambridge University
601 Press. <https://doi.org/10.1017/CBO9781139020138.002>
- 602 Cherkose, B. A., & Saibi, H. (2021). Investigation of the Ayrobera geothermal field using 3D
603 magnetotelluric data inversion, Afar depression, NE Ethiopia. *Geothermics*, *94*, 102114.
604 <https://doi.org/10.1016/j.geothermics.2021.102114>
- 605 Comeau, M. J., Becken, M., Connolly, J. A. D., Grayver, A. V., & Kuvshinov, A. V. (2020).
606 Compaction - driven fluid localization as an explanation for lower crustal electrical
607 conductors in an intracontinental setting. *Geophysical Research Letters*, *47*(19),
608 e2020GL088455. <https://doi.org/10.1029/2020GL088455>
- 609 Constable, S., Parker, R. L., & Constable, C. G. (1987). Occam's inversion: A practical algorithm
610 for generating smooth models from electromagnetic sounding data. *Geophysics*, *52*(3), 289–
611 300. <https://doi.org/10.1190/1.1442303>
- 612 Cordell, D., Unsworth, M. J., Lee, B., Díaz, D., Bennington, N. L., & Thurber, C. H. (2020).
613 Integrating magnetotelluric and seismic images of silicic magma systems: A case study from
614 the Laguna del Maule Volcanic Field, central Chile. *Journal of Geophysical Research: Solid*
615 *Earth*, *125*(11), e2020JB020459. <https://doi.org/10.1029/2020JB020459>
- 616 Di Paolo, F., Ledo, J., Ślęzak, K., Martínez van Dorth, D., Cabrera-Pérez, I., & Pérez, N. M.
617 (2020). La Palma island (Spain) geothermal system revealed by 3D magnetotelluric data
618 inversion. *Scientific Reports*, *10*(1), 18181. <https://doi.org/10.1038/s41598-020-75001-z>
- 619 Doi, N., Kato, O., Ikeuchi, K., Komatsu, R., Miyazaki, S., Akaku, K., & Uchida, T. (1998).
620 Genesis of the plutonic-hydrothermal system around quaternary granite in the kakkonda
621 geothermal system, Japan. *Geothermics*, *27*(5), 663–690. [https://doi.org/10.1016/S0375-6505\(98\)00039-X](https://doi.org/10.1016/S0375-6505(98)00039-X)
- 623 Driesner, T., & Heinrich, C. A. (2007). The system H₂O–NaCl. Part I: Correlation formulae for
624 phase relations in temperature–pressure–composition space from 0 to 1000°C, 0 to 5000bar,
625 and 0 to 1 XNaCl. *Geochimica et Cosmochimica Acta*, *71*(20), 4880–4901.
626 <https://doi.org/10.1016/j.gca.2006.01.033>
- 627 Elders, W. A., Friðleifsson, G. Ó., & Albertsson, A. (2014). Drilling into magma and the
628 implications of the Iceland Deep Drilling Project (IDDP) for high-temperature geothermal
629 systems worldwide. *Geothermics*, *49*, 111–118.
630 <https://doi.org/10.1016/j.geothermics.2013.05.001>
- 631 Farquharson, C. G. (2008). Constructing piecewise-constant models in multidimensional
632 minimum-structure inversions. *Geophysics*, *73*(1), K1–K9. <https://doi.org/10.1190/1.2816650>
- 633 Feucht, D. W., Sheehan, A. F., & Bedrosian, P. A. (2017). Magnetotelluric imaging of lower
634 crustal melt and lithospheric hydration in the Rocky Mountain Front transition zone, Colorado,
635 USA. *Journal of Geophysical Research: Solid Earth*, *122*(12), 9489–9510.
636 <https://doi.org/10.1002/2017JB014474>
- 637 Fournier, R. O. (1999). Hydrothermal processes related to movement of fluid from plastic into
638 brittle rock in the magmatic-epithermal environment. *Economic Geology*, *94*(8), 1193–1211.
639 <https://doi.org/10.2113/gsecongeo.94.8.1193>
- 640 Friðleifsson, G. Ó., Elders, W. A., Zierenberg, R. A., Fowler, A. P. G., Weisenberger, T. B.,
641 Mesfin, K. G., et al. (2020). The Iceland Deep Drilling Project at Reykjanes: Drilling into the
642 root zone of a black smoker analog. *Journal of Volcanology and Geothermal Research*, *391*,
643 106435. <https://doi.org/10.1016/j.jvolgeores.2018.08.013>
- 644 Gaillard, F., & Marziano, G. I. (2005). Electrical conductivity of magma in the course of

- 645 crystallization controlled by their residual liquid composition. *Journal of Geophysical*
646 *Research: Solid Earth*, 110(B6). <https://doi.org/10.1029/2004JB003282>
- 647 Gresse, M., Uyeshima, M., Koyama, T., Hase, H., Aizawa, K., Yamaya, Y., et al. (2021).
648 Hydrothermal and magmatic system of a volcanic island inferred from magnetotellurics,
649 seismicity, self-potential, and thermal image: an example of Miyakejima (Japan). *Journal of*
650 *Geophysical Research: Solid Earth*, 126(6), e2021JB022034.
651 <https://doi.org/10.1029/2021JB022034>
- 652 Guo, X., Li, B., Ni, H., & Mao, Z. (2017). Electrical conductivity of hydrous andesitic melts
653 pertinent to subduction zones. *Journal of Geophysical Research: Solid Earth*, 122(3), 1777–
654 1788. <https://doi.org/10.1002/2016JB013524>
- 655 Hasegawa, A., Zhao, D., Hori, S., Yamamoto, A., & Horiuchi, S. (1991). Deep structure of the
656 northeastern Japan arc and its relationship to seismic and volcanic activity. *Nature*, 352(6337),
657 683–689. <https://doi.org/10.1038/352683a0>
- 658 Hashin, Z., & Shtrikman, S. (1962). A variational approach to the theory of the effective magnetic
659 permeability of multiphase materials. *Journal of Applied Physics*, 33(10), 3125–3131.
660 <https://doi.org/10.1063/1.1728579>
- 661 Hata, M., Oshiman, N., Yoshimura, R., Tanaka, Y., & Uyeshima, M. (2015). Three-dimensional
662 electromagnetic imaging of upwelling fluids in the Kyushu subduction zone, Japan. *Journal*
663 *of Geophysical Research: Solid Earth*, 120(1), 1–17. <https://doi.org/10.1002/2014JB011336>
- 664 Heinrich, C. A. (2005). The physical and chemical evolution of low-salinity magmatic fluids at the
665 porphyry to epithermal transition: a thermodynamic study. *Mineralium Deposita*, 39(8), 864–
666 889. <https://doi.org/10.1007/s00126-004-0461-9>
- 667 Heinson, G., Didana, Y., Soeffky, P., Thiel, S., & Wise, T. (2018). The crustal geophysical
668 signature of a world-class magmatic mineral system. *Scientific Reports*, 8(1), 10608.
669 <https://doi.org/10.1038/s41598-018-29016-2>
- 670 Heise, W., Caldwell, T. G., Bibby, H. M., & Bannister, S. C. (2008). Three-dimensional modelling
671 of magnetotelluric data from the Rotokawa geothermal field, Taupo Volcanic Zone, New
672 Zealand. *Geophysical Journal International*, 173(2), 740–750. <https://doi.org/10.1111/j.1365-246X.2008.03737.x>
- 674 Hill, G. J., Caldwell, T. G., Heise, W., Chertkoff, D. G., Bibby, H. M., Burgess, M. K., et al.
675 (2009). Distribution of melt beneath Mount St Helens and Mount Adams inferred from
676 magnetotelluric data. *Nature Geoscience*, 2(11), 785–789. <https://doi.org/10.1038/ngeo661>
- 677 Horiguchi, K., Ueki, S., Sano, Y., Takahata, N., Hasegawa, A., & Igarashi, G. (2010).
678 Geographical distribution of helium isotope ratios in northeastern Japan. *Island Arc*, 19(1),
679 60–70. <https://doi.org/10.1111/j.1440-1738.2009.00703.x>
- 680 Hyndman, R. D., & Shearer, P. M. (1989). Water in the lower continental crust: modelling
681 magnetotelluric and seismic reflection results. *Geophysical Journal International*, 98(2), 343–
682 365. <https://doi.org/10.1111/j.1365-246X.1989.tb03357.x>
- 683 Ichihara, H., Mogi, T., Tanimoto, K., Yamaya, Y., Hashimoto, T., Uyeshima, M., & Ogawa, Y.
684 (2016). Crustal structure and fluid distribution beneath the southern part of the Hidaka
685 collision zone revealed by 3-D electrical resistivity modeling. *Geochemistry, Geophysics,*
686 *Geosystems*, 17(4), 1480–1491. <https://doi.org/10.1002/2015GC006222>
- 687 Ichiki, M., Kaida, T., Nakayama, T., Miura, S., Yamamoto, M., Morita, Y., & Uyeshima, M.
688 (2021). Magma reservoir beneath Azumayama Volcano, NE Japan, as inferred from a three-
689 dimensional electrical resistivity model explored by means of magnetotelluric method. *Earth,*
690 *Planets and Space*, 73(1), 150. <https://doi.org/10.1186/s40623-021-01451-y>

- 691 Ikeuchi, K., Doi, N., Sakagawa, Y., Kamenosono, H., & Uchida, T. (1998). High-temperature
 692 measurements in well WD-1A and the thermal structure of the kakkonda geothermal system,
 693 Japan. *Geothermics*, 27(5), 591–607. [https://doi.org/10.1016/S0375-6505\(98\)00035-2](https://doi.org/10.1016/S0375-6505(98)00035-2)
- 694 Ingebritsen, S. E., & Manning, C. E. (2010). Permeability of the continental crust: dynamic
 695 variations inferred from seismicity and metamorphism. *Geofluids*, 10(1-2), 193–205.
 696 <https://doi.org/10.1111/j.1468-8123.2010.00278.x>
- 697 Ingham, M. R., Bibby, H. M., Heise, W., Jones, K. A., Cairns, P., Dravitzki, S., et al. (2009). A
 698 magnetotelluric study of Mount Ruapehu volcano, New Zealand. *Geophysical Journal
 699 International*, 179(2), 887–904. <https://doi.org/10.1111/j.1365-246X.2009.04317.x>
- 700 Ishizu, K., Ogawa, Y., Mogi, T., Yamaya, Y., & Uchida, T. (2021). Ability of the magnetotelluric
 701 method to image a deep conductor: Exploration of a supercritical geothermal system.
 702 *Geothermics*, 96, 102205. <https://doi.org/10.1016/j.geothermics.2021.102205>
- 703 Kanda, W., Utsugi, M., Takakura, S., & Inoue, H. (2019). Hydrothermal system of the active crater
 704 of Aso volcano (Japan) inferred from a three-dimensional resistivity structure model. *Earth,
 705 Planets and Space*, 71(1), 37. <https://doi.org/10.1186/s40623-019-1017-7>
- 706 Kawamoto, T., Yoshikawa, M., Kumagai, Y., Mirabueno, M. H. T., Okuno, M., & Kobayashi, T.
 707 (2013). Mantle wedge infiltrated with saline fluids from dehydration and decarbonation of
 708 subducting slab. *Proceedings of the National Academy of Sciences of the United States of
 709 America*, 110(24), 9663–9668. <https://doi.org/10.1073/pnas.1302040110>
- 710 Kelbert, A., Meqbel, N., Egbert, G. D., & Tandon, K. (2014). ModEM: A modular system for
 711 inversion of electromagnetic geophysical data. *Computers & Geosciences*, 66, 40–53.
 712 <https://doi.org/10.1016/j.cageo.2014.01.010>
- 713 Kita, I., Nagao, K., Nakamura, Y., & Taguchi, S. (1992). Information on geothermal system
 714 obtained by chemical and isotropic charactics of soil and fumarolic gases from the Doroyu-
 715 Kawarage geothermal field, Akita, Japan. *Journal of the Geothermal Research Society of
 716 Japan*, 14(2), 115–128 (in Japanese). <https://doi.org/10.11367/grsj1979.14.115>
- 717 Laumonier, M., Gaillard, F., & Sifre, D. (2015). The effect of pressure and water concentration on
 718 the electrical conductivity of dacitic melts: Implication for magnetotelluric imaging in
 719 subduction areas. *Chemical Geology*, 418, 66–76.
 720 <https://doi.org/10.1016/j.chemgeo.2014.09.019>
- 721 Le Pape, F., Jones, A. G., Unsworth, M. J., Vozar, J., Wei, W., Jin, S., et al. (2015). Constraints on
 722 the evolution of crustal flow beneath Northern Tibet. *Geochemistry, Geophysics, Geosystems*,
 723 16(12), 4237–4260. <https://doi.org/10.1002/2015GC005828>
- 724 Ledo, J., García-Merino, M., Larnier, H., Slezak, K., Piña-Varas, P., Marcuello, A., et al. (2021).
 725 3D electrical resistivity of Gran Canaria island using magnetotelluric data. *Geothermics*, 89,
 726 101945. <https://doi.org/10.1016/j.geothermics.2020.101945>
- 727 Lee, B., Unsworth, M., Árnason, K., & Cordell, D. (2020). Imaging the magmatic system beneath
 728 the Krafla geothermal field, Iceland: A new 3-D electrical resistivity model from inversion of
 729 magnetotelluric data. *Geophysical Journal International*, 220(1), 541–567.
 730 <https://doi.org/10.1093/gji/ggz427>
- 731 Lowell, R. P., Van Cappellen, P., & Germanovich, L. N. (1993). Silica precipitation in fractures
 732 and the evolution of permeability in hydrothermal upflow zones. *Science*, 260(5105), 192.
 733 <https://doi.org/10.1126/science.260.5105.192>
- 734 Manning, C. E. (1994). The solubility of quartz in H₂O in the lower crust and upper mantle.
 735 *Geochimica et Cosmochimica Acta*, 58(22), 4831–4839. [https://doi.org/10.1016/0016-7037\(94\)90214-3](https://doi.org/10.1016/0016-7037(94)90214-3)
- 736

- 737 Mitsuhashi, Y., Ogawa, Y., Mishina, M., Kono, T., Yokokura, T., & Uchida, T. (2001).
738 Electromagnetic heterogeneity of the seismogenic region of 1962 M6.5 Northern Miyagi
739 Earthquake, northeastern Japan. *Geophysical Research Letters*, 28(23), 4371–4374.
740 <https://doi.org/10.1029/2001GL013079>
- 741 Monecke, T., Monecke, J., Reynolds, T. J., Tsuruoka, S., Bennett, M. M., Skewes, W. B., & Palin,
742 R. M. (2018). Quartz solubility in the H₂O-NaCl system: A framework for understanding
743 vein formation in porphyry copper deposits. *Economic Geology*, 113(5), 1007–1046.
744 <https://doi.org/10.5382/econgeo.2018.4580>
- 745 Moorkamp, M., Fishwick, S., Walker, R. J., & Jones, A. G. (2019). Geophysical evidence for
746 crustal and mantle weak zones controlling intra-plate seismicity – the 2017 Botswana
747 earthquake sequence. *Earth and Planetary Science Letters*, 506, 175–183.
748 <https://doi.org/10.1016/j.epsl.2018.10.048>
- 749 Muraoka, H., Uchida, T., Sasada, M., Yagi, M., Akaku, K., Sasaki, M., et al. (1998). Deep
750 geothermal resources survey program: igneous, metamorphic and hydrothermal processes in a
751 well encountering 500°C at 3729 m depth, Kakkonda, Japan. *Geothermics*, 27(5), 507–534.
752 [https://doi.org/10.1016/S0375-6505\(98\)00031-5](https://doi.org/10.1016/S0375-6505(98)00031-5)
- 753 Nakajima, J., Matsuzawa, T., Hasegawa, A., & Zhao, D. (2001). Seismic imaging of arc magma
754 and fluids under the central part of northeastern Japan. *Tectonophysics*, 341(1), 1–17.
755 [https://doi.org/10.1016/S0040-1951\(01\)00181-0](https://doi.org/10.1016/S0040-1951(01)00181-0)
- 756 New Energy and Industrial Technology Development Organization. (1990). Final report on survey
757 to identify and promote geothermal development at Minase field, 1121 pp (in Japanese).
758 Retrieved from <https://geothermal.jogmec.go.jp/report/nedo/file/30.pdf>
- 759 Newman, G. A. (2014). A Review of High-Performance Computational Strategies for Modeling
760 and Imaging of Electromagnetic Induction Data. *Surveys in Geophysics*, 35(1), 85–100.
761 <https://doi.org/10.1007/s10712-013-9260-0>
- 762 Nono, F., Gibert, B., Parat, F., Loggia, D., Cichy, S. B., & Violay, M. (2020). Electrical
763 conductivity of Icelandic deep geothermal reservoirs up to supercritical conditions: Insight
764 from laboratory experiments. *Journal of Volcanology and Geothermal Research*, 391, 106364.
765 <https://doi.org/10.1016/j.jvolgeores.2018.04.021>
- 766 Nunohara, K., Okano, H., Yamada, R., Hirano, N., & Tsuchiya, N. (2021). Geothermal potentiality
767 in southern part of the Sanzugawa Caldera, Akita prefecture, Northeast Japan. *Journal of the*
768 *Geothermal Research Society of Japan*, 24(4), 313–314 (in Japanese).
- 769 Ogawa, Y., & Uchida, T. (1996). A two-dimensional magnetotelluric inversion assuming Gaussian
770 static shift. *Geophysical Journal International*, 126(1), 69–76. <https://doi.org/10.1111/j.1365-246X.1996.tb05267.x>
- 771
- 772 Ogawa, Y., Mishina, M., Goto, T., Satoh, H., Oshiman, N., Kasaya, T., et al. (2001).
773 Magnetotelluric imaging of fluids in intraplate earthquake zones, NE Japan Back Arc.
774 *Geophysical Research Letters*, 28(19), 3741–3744. <https://doi.org/10.1029/2001GL013269>
- 775 Ogawa, Y., Ichiki, M., Kanda, W., Mishina, M., & Asamori, K. (2014). Three-dimensional
776 magnetotelluric imaging of crustal fluids and seismicity around Naruko volcano, NE Japan.
777 *Earth, Planets and Space*, 66(1), 158. <https://doi.org/10.1186/s40623-014-0158-y>
- 778 Okada, T., Matsuzawa, T., Nakajima, J., Uchida, N., Yamamoto, M., Hori, S., et al. (2014).
779 Seismic velocity structure in and around the Naruko volcano, NE Japan, and its implications
780 for volcanic and seismic activities. *Earth, Planets and Space*, 66(1), 114.
781 <https://doi.org/10.1186/1880-5981-66-114>
- 782 Okamoto, K., Asanuma, H., Ishibashi, T., Yamaya, Y., Saishu, H., Yanagisawa, N., et al. (2019).

- 783 Geological and engineering features of developing ultra-high-temperature geothermal systems
784 in the world. *Geothermics*, 82, 267–281. <https://doi.org/10.1016/j.geothermics.2019.07.002>
- 785 Parisio, F., Vilarrasa, V., Wang, W., Kolditz, O., & Nagel, T. (2019). The risks of long-term re-
786 injection in supercritical geothermal systems. *Nature Communications*, 10(1), 4391.
787 <https://doi.org/10.1038/s41467-019-12146-0>
- 788 Peacock, J. R., Mangan, M. T., McPhee, D., & Ponce, D. A. (2015). Imaging the magmatic system
789 of Mono Basin, California, with magnetotellurics in three dimensions. *Journal of Geophysical*
790 *Research: Solid Earth*, 120(11), 7273–7289. <https://doi.org/10.1002/2015JB012071>
- 791 Peacock, J. R., Earney, T. E., Mangan, M. T., Schermerhorn, W. D., Glen, J. M., Walters, M., &
792 Hartline, C. (2020). Geophysical characterization of the Northwest Geysers geothermal field,
793 California. *Journal of Volcanology and Geothermal Research*, 399, 106882.
794 <https://doi.org/10.1016/j.jvolgeores.2020.106882>
- 795 Piana Agostinetti, N., Licciardi, A., Piccinini, D., Mazzarini, F., Musumeci, G., Saccorotti, G., &
796 Chiarabba, C. (2017). Discovering geothermal supercritical fluids: a new frontier for seismic
797 exploration. *Scientific Reports*, 7(1), 14592. <https://doi.org/10.1038/s41598-017-15118-w>
- 798 Piña-Varas, P., Ledo, J., Queralt, P., Marcuello, A., & Perez, N. (2018). On the detectability of
799 Teide volcano magma chambers (Tenerife, Canary Islands) with magnetotelluric data. *Earth,*
800 *Planets and Space*, 70(1), 14. <https://doi.org/10.1186/s40623-018-0783-y>
- 801 Pommier, A., & Le-Trong, E. (2011). “SIGMELTS”: A web portal for electrical conductivity
802 calculations in geosciences. *Computers & Geosciences*, 37(9), 1450–1459.
803 <https://doi.org/10.1016/j.cageo.2011.01.002>
- 804 Quist, A. S., & Marshall, W. L. (1968). Electrical conductances of aqueous sodium chloride
805 solutions from 0 to 800. degree. and at pressures to 4000 bars. *The Journal of Physical*
806 *Chemistry*, 72(2), 684–703. <https://doi.org/10.1021/j100848a050>
- 807 Reinsch, T., Dobson, P., Asanuma, H., Huenges, E., Poletto, F., & Sanjuan, B. (2017). Utilizing
808 supercritical geothermal systems: a review of past ventures and ongoing research activities.
809 *Geothermal Energy*, 5(1), 16. <https://doi.org/10.1186/s40517-017-0075-y>
- 810 Revil, A., Qi, Y., Ghorbani, A., Coperey, A., Ahmed, A. S., Finizola, A., & Ricci, T. (2019).
811 Induced polarization of volcanic rocks. 3. Imaging clay cap properties in geothermal fields.
812 *Geophysical Journal International*, 218(2), 1398–1427. <https://doi.org/10.1093/gji/ggz207>
- 813 Richards, J. P. (2011). Magmatic to hydrothermal metal fluxes in convergent and collided margins.
814 *Ore Geology Reviews*, 40(1), 1–26. <https://doi.org/10.1016/j.oregeorev.2011.05.006>
- 815 Saishu, H., Okamoto, A., & Tsuchiya, N. (2014). The significance of silica precipitation on the
816 formation of the permeable–impermeable boundary within Earth’s crust. *Terra Nova*, 26(4),
817 253–259. <https://doi.org/10.1111/ter.12093>
- 818 Sakuma, H., & Ichiki, M. (2016). Electrical conductivity of NaCl-H₂O fluid in the crust. *Journal*
819 *of Geophysical Research: Solid Earth*, 121(2), 577–594.
820 <https://doi.org/10.1002/2015JB012219>
- 821 Samrock, F., Grayver, A. V., Eysteinnsson, H., & Saar, M. O. (2018). Magnetotelluric image of
822 transcrustal magmatic system beneath the Tulu Moye geothermal prospect in the Ethiopian
823 Rift. *Geophysical Research Letters*, 45(23), 12,847–12,855.
824 <https://doi.org/10.1029/2018GL080333>
- 825 Scholz, C. H. (2019). *The Mechanics of Earthquakes and Faulting* (3rd ed.). Cambridge:
826 Cambridge University Press. <https://doi.org/10.1017/9781316681473>
- 827 Scott, S., Driesner, T., & Weis, P. (2015). Geologic controls on supercritical geothermal resources
828 above magmatic intrusions. *Nature Communications*, 6(1), 7837.

- 829 <https://doi.org/10.1038/ncomms8837>
- 830 Sibson, R. H. (2020). Preparation zones for large crustal earthquakes consequent on fault-valve
831 action. *Earth, Planets and Space*, 72(1), 31. <https://doi.org/10.1186/s40623-020-01153-x>
- 832 Sillitoe, R. H. (2010). Porphyry copper systems. *Economic Geology*, 105(1), 3–41.
833 <https://doi.org/10.2113/gsecongeo.105.1.3>
- 834 Sinmyo, R., & Keppler, H. (2016). Electrical conductivity of NaCl-bearing aqueous fluids to
835 600 °C and 1 GPa. *Contributions to Mineralogy and Petrology*, 172(1), 4.
836 <https://doi.org/10.1007/s00410-016-1323-z>
- 837 Siripunvaraporn, W., & Egbert, G. (2009). WSINV3DMT: Vertical magnetic field transfer
838 function inversion and parallel implementation. *Physics of the Earth and Planetary Interiors*,
839 173(3), 317–329. <https://doi.org/10.1016/j.pepi.2009.01.013>
- 840 Siripunvaraporn, W., Egbert, G., Lenbury, Y., & Uyeshima, M. (2005). Three-dimensional
841 magnetotelluric inversion: data-space method. *Physics of the Earth and Planetary Interiors*,
842 150(1–3), 3–14. <https://doi.org/10.1016/j.pepi.2004.08.023>
- 843 Stimac, J., Wilmarth, M., Mandeno, P. E., Dobson, P., & Winick, J. (2017). Review of exploitable
844 supercritical geothermal resources to 5 km at Geysers-Clear Lake, Salton Sea, and Coso. *GRC*
845 *Transactions*, 41, 806–835. Retrieved from
846 <https://publications.mygeoenergynow.org/grc/1033767.pdf>
- 847 Takeno, N. (2000). Thermal and geochemical structure of the Uenotai geothermal system, Japan.
848 *Geothermics*, 29(2), 257–277. [https://doi.org/10.1016/S0375-6505\(99\)00062-0](https://doi.org/10.1016/S0375-6505(99)00062-0)
- 849 Tamanyu, S., Fujiwara, S., Ishikawa, J., & Jingu, H. (1998). Fracture system related to geothermal
850 reservoir based on core samples of slim holes. Example from the Uenotai geothermal field,
851 northern Honshu, Japan. *Geothermics*, 27(2), 143–166. [https://doi.org/10.1016/S0375-6505\(97\)10012-8](https://doi.org/10.1016/S0375-6505(97)10012-8)
- 852
- 853 Tamura, Y., Tatsumi, Y., Zhao, D., Kido, Y., & Shukuno, H. (2002). Hot fingers in the mantle
854 wedge: new insights into magma genesis in subduction zones. *Earth and Planetary Science*
855 *Letters*, 197(1), 105–116. [https://doi.org/10.1016/S0012-821X\(02\)00465-X](https://doi.org/10.1016/S0012-821X(02)00465-X)
- 856 Tatsumi, Y., Takahashi, T., Hirahara, Y., Chang, Q., Miyazaki, T., Kimura, J.-I., et al. (2008). New
857 insights into andesite genesis: the role of mantle-derived calc-alkalic and crust-derived
858 tholeiitic melts in magma differentiation beneath Zao Volcano, NE Japan. *Journal of*
859 *Petrology*, 49(11), 1971–2008. <https://doi.org/10.1093/petrology/egn055>
- 860 Tatsumi, Y. (1989). Migration of fluid phases and genesis of basalt magmas in subduction zones.
861 *Journal of Geophysical Research: Solid Earth*, 94(B4), 4697–4707.
862 <https://doi.org/10.1029/JB094iB04p04697>
- 863 Tseng, K. H., Ogawa, Y., Nurhasan, Tank, S. B., Ujihara, N., Honkura, Y., et al. (2020). Anatomy
864 of active volcanic edifice at the Kusatsu–Shirane volcano, Japan, by magnetotellurics:
865 hydrothermal implications for volcanic unrests. *Earth, Planets and Space*, 72(1), 161.
866 <https://doi.org/10.1186/s40623-020-01283-2>
- 867 Tsuchiya, N., & Hirano, N. (2007). Chemical reaction diversity of geofluids revealed by
868 hydrothermal experiments under sub- and supercritical states. *Island Arc*, 16(1), 6–15.
869 <https://doi.org/10.1111/j.1440-1738.2007.00554.x>
- 870 Tsuchiya, N., Yamada, R., & Uno, M. (2016). Supercritical geothermal reservoir revealed by a
871 granite–porphyry system. *Geothermics*, 63, 182–194.
872 <https://doi.org/10.1016/j.geothermics.2015.12.011>
- 873 Tuttle, O. F., & Bowen, N. L. (1958). Origin of granite in the light of experimental studies in the
874 system NaAlSi₃O₈–KAlSi₃O₈–SiO₂–H₂O. In O. F. Tuttle & N. L. Bowen (Eds.), *Origin of*

- 875 *Granite in the Light of Experimental Studies in the System NaAlSi₃O₈–KAlSi₃O₈–SiO₂–H₂O*
876 (Vol. 74, p. 0). Geological Society of America. <https://doi.org/10.1130/MEM74-p1>
- 877 Umeda, K., Hayashi, S., & Ban, M. (1999). K-Ar ages of Zarumori, Takamatsu, Funagata and
878 Sankichi-Hayama volcanoes, NE Japan. *Bulletin of the Volcanological Society of Japan*, 44(4),
879 217–222 (in Japanese). https://doi.org/10.18940/kazan.44.4_217
- 880 Unsworth, M. J., Jones, A. G., Wei, W., Marquis, G., Gokarn, S. G., Spratt, J. E., et al. (2005).
881 Crustal rheology of the Himalaya and Southern Tibet inferred from magnetotelluric data.
882 *Nature*, 438(7064), 78–81. <https://doi.org/10.1038/nature04154>
- 883 Ussher, G., Harvey, C., Johnstone, R., & Anderson, E. (2000). Understanding the resistivities
884 observed in geothermal systems. In *proceedings world geothermal congress* (pp. 1915–1920).
885 Kyushu. Retrieved from [https://www.geothermal-](https://www.geothermal-energy.org/pdf/IGASstandard/WGC/2000/R0279.PDF)
886 [energy.org/pdf/IGASstandard/WGC/2000/R0279.PDF](https://www.geothermal-energy.org/pdf/IGASstandard/WGC/2000/R0279.PDF)
- 887 Wallace, P. J. (2005). Volatiles in subduction zone magmas: concentrations and fluxes based on
888 melt inclusion and volcanic gas data. *Journal of volcanology and Geothermal Research*,
889 140(1), 217–240. <https://doi.org/10.1016/j.jvolgeores.2004.07.023>
- 890 Wannamaker, P. E., Caldwell, T. G., Jiracek, G. R., Maris, V., Hill, G. J., Ogawa, Y., et al. (2009).
891 Fluid and deformation regime of an advancing subduction system at Marlborough, New
892 Zealand. *Nature*, 460(7256), 733–736. <https://doi.org/10.1038/nature08204>
- 893 Watanabe, N., Numakura, T., Sakaguchi, K., Saishu, H., Okamoto, A., Ingebritsen, S. E., &
894 Tsuchiya, N. (2017). Potentially exploitable supercritical geothermal resources in the ductile
895 crust. *Nature Geoscience*, 10(2), 140–144. <https://doi.org/10.1038/ngeo2879>
- 896 Watanabe, T., & Peach, C. J. (2002). Electrical impedance measurement of plastically deforming
897 halite rocks at 125°C and 50 MPa. *Journal of Geophysical Research: Solid Earth*, 107(B1),
898 ECV 2-1-ECV 2-12. <https://doi.org/10.1029/2001JB000204>
- 899 Weatherley, D., & Henley, R. (2013). Flash vaporization during earthquakes evidenced by gold
900 deposits. *Nature Geoscience*, 6, 294–298. <https://doi.org/10.1038/ngeo1759>
- 901 Weis, P., Driesner, T., & Heinrich, C. A. (2012). Porphyry-copper ore shells form at stable
902 pressure-temperature fronts within dynamic fluid plumes. *Science*, 338(6114), 1613.
903 <https://doi.org/10.1126/science.1225009>
- 904 Wersin, P., Johnson, L. H., & McKinley, I. G. (2007). Performance of the bentonite barrier at
905 temperatures beyond 100°C: A critical review. *Physics and Chemistry of the Earth*, 32(8),
906 780–788. <https://doi.org/10.1016/j.pce.2006.02.051>
- 907 Wise, T., & Thiel, S. (2020). Proterozoic tectonothermal processes imaged with magnetotellurics
908 and seismic reflection in southern Australia. *Geoscience Frontiers*, 11(3), 885–893.
909 <https://doi.org/10.1016/j.gsf.2019.09.006>
- 910 Yamaya, Y., Alanis, P. K. B., Takeuchi, A., Cordon, J. M., Mogi, T., Hashimoto, T., et al. (2013).
911 A large hydrothermal reservoir beneath Taal Volcano (Philippines) revealed by
912 magnetotelluric resistivity survey: 2D resistivity modeling. *Bulletin of Volcanology*, 75(7),
913 729. <https://doi.org/10.1007/s00445-013-0729-y>
- 914 Yamaya, Y., Mogi, T., Honda, R., Hase, H., Hashimoto, T., & Uyeshima, M. (2017). Three-
915 dimensional resistivity structure in Ishikari Lowland, Hokkaido, northeastern Japan—
916 Implications to strain concentration mechanism. *Geochemistry, Geophysics, Geosystems*,
917 18(2), 735–754. <https://doi.org/10.1002/2016GC006771>
- 918 Yoshida, T., Kimura, J.-I., Yamada, R., Acocella, V., Sato, H., Zhao, D., et al. (2014). Evolution of
919 late Cenozoic magmatism and the crust–mantle structure in the NE Japan Arc. *Geological*
920 *Society, London, Special Publications*, 385(1), 335. <https://doi.org/10.1144/SP385.15>

921 Yoshimura, R., Ogawa, Y., Yukutake, Y., Kanda, W., Komori, S., Hase, H., et al. (2018).
922 Resistivity characterisation of Hakone volcano, Central Japan, by three-dimensional
923 magnetotelluric inversion. *Earth, Planets and Space*, 70(1), 66.
924 <https://doi.org/10.1186/s40623-018-0848-y>